



Dynamic degradation patterns of porous polycaprolactone/ β -tricalcium phosphate composites orchestrate macrophage responses and immunoregulatory bone regeneration

Hao Wu^{a,1}, Xinghui Wei^{a,1}, Yichao Liu^{b,1}, Hui Dong^b, Zhen Tang^a, Ning Wang^a, Shusen Bao^a, Zhigang Wu^c, Lei Shi^b, Xiongfei Zheng^d, Xiaokang Li^{a,**}, Zheng Guo^{a,*}

^a Department of Orthopaedics, Tangdu Hospital, Fourth Military Medical University, Xi'an, Shaanxi, 710038, PR China

^b Department of Orthopaedics, Xijing Hospital, Fourth Military Medical University, Xi'an, Shaanxi, 710032, PR China

^c Department of Orthopaedics, The 63750 Hospital of People's Liberation Army, Xi'an, Shaanxi, 710038, PR China

^d State Key Laboratory of Robotics, Shenyang Institute of Automation, Chinese Academy of Sciences, Shenyang, Liaoning, 110000, PR China

ARTICLE INFO

Keywords:

Polycaprolactone/ β -TCP
Dynamic degradation
Macrophage response
Bone healing

ABSTRACT

Biodegradable polycaprolactone/ β -tricalcium phosphate (PT) composites are desirable candidates for bone tissue engineering applications. A higher β -tricalcium phosphate (TCP) ceramic content improves the mechanical, hydrophilic and osteogenic properties of PT scaffolds *in vitro*. Using a dynamic degradation reactor, we established a steady *in vitro* degradation model to investigate the changes in the physio-chemical and biological properties of PT scaffolds during degradation. PT46 and PT37 scaffolds underwent degradation more rapidly than PT scaffolds with lower TCP contents. *In vivo* studies revealed the rapid degradation of PT (PT46 and PT37) scaffolds disturbed macrophage responses and lead to bone healing failure. Macrophage co-culture assays and a subcutaneous implantation model indicated that the scaffold degradation process dynamically affected macrophage responses, especially polarization. RNA-Seq analysis indicated phagocytosis of the degradation products of PT37 scaffolds induces oxidative stress and inflammatory M1 polarization in macrophages. Overall, this study reveals that the dynamic patterns of biodegradation of degradable bone scaffolds highly orchestrate immune responses and thus determine the success of bone regeneration. Therefore, through evaluation of the biological effects of biomaterials during the entire process of degradation on immune responses and bone regeneration are necessary in order to develop more promising biomaterials for bone regeneration.

1. Introduction

Bone tissue engineering (BTE) is a promising strategy for treating bone defects when the defect zone exceeds the critical size for the self-healing capacity of bone [1]. Scaffolds fabricated with various materials can serve as components of extracellular matrix (ECM) and provide an appropriate microenvironment for cellular adhesion and bone ingrowth [2,3]. Compared with bioinert materials, biodegradable materials are considered as better candidates for bone tissue engineering as they are resorbed by surrounding tissues and ultimately replaced by natural bone structures [4,5]. Define PCL and PCL-based scaffolds have

been approved by the Food and Drug Administration (FDA) and widely used as tissue engineering scaffolds [6,7]. However, due to the lack of bioactive agents, materials made of PCL alone are rarely used as bone tissue engineering scaffolds. Thus, other biological components such as ceramics, metals, bioactive factors and drugs are incorporated into PCL scaffolds to enhance their biological properties [8–10]. The combination of bio-ceramics with PCL not only effectively neutralizes the acidic byproducts of scaffold degradation, but also enhances the degradability of the scaffolds and augments their bone regenerative effects [11–13].

Calcium phosphate-based bio-ceramics such as hydroxyapatite and tricalcium phosphate (TCP) can significantly enhance the

Peer review under responsibility of KeAi Communications Co., Ltd.

* Corresponding author.

** Corresponding author.

E-mail addresses: lxkfmumu@163.com (X. Li), guozheng@fmmu.edu.cn (Z. Guo).

¹ These authors contributed equally to this paper.

<https://doi.org/10.1016/j.bioactmat.2022.07.032>

Received 14 June 2022; Received in revised form 17 July 2022; Accepted 24 July 2022

Available online 6 August 2022

2452-199X/© 2022 The Authors. Publishing services by Elsevier B.V. on behalf of KeAi Communications Co. Ltd. This is an open access article under the CC BY-NC-ND license (<http://creativecommons.org/licenses/by-nc-nd/4.0/>).

biocompatibility and osteoconductivity of polymer scaffolds [14,15]. TCP is commonly used in bone tissue engineering due to its fast degradation rate and ability to induce bone-material bonding. Researchers have also reported that TCP can stimulate macrophage responses and promote osteogenesis [16]. In our previous studies, we fabricated a biodegradable polycaprolactone-tricalcium phosphate (PCL/TCP; 80/20 composition) scaffold as spinal fusion cage using a fused deposition modeling (FDM) technique. The PCL/TCP scaffolds achieved barely satisfactory osteointegration *in vivo*, but the in-growth of inner bone was not significant and may limit further application of these composite scaffolds in bone repair [17]. Studies have shown that incorporation of higher ceramic contents into scaffolds may improve the osteogenic differentiation of osteoblasts and bone healing effects *in vivo* [18–20]. Thus, our group further increased the TCP mass ratio and 3D printed a range of blended PCL/ β -TCP composite scaffolds with a balanced mass fraction (70/30 to 30/70 w/w).

Many researchers have demonstrated that the mechanical strength, hydrophilicity and degradability of polymer-based composites were improved when the ceramic ratio is enhanced [11,21,22]. The degradability highly influences both scaffold degradation and the bone regeneration process. In our previous studies, we found that new bone formation dynamically synchronizes with the degradation of PCL/TCP scaffolds (80/20) and that a relatively slow degradation rate may hinder the long-term bone ingrowth. Based on this finding, the improved degradability of PCL/TCP scaffolds with higher ceramic contents may also enhance new bone formation and substitution. Many other researchers have also focused on tailoring the degradability of materials to control biological processes and improve bone repair [23–25]. However, the scaffold degradation process is a “double edged sword” during bone regeneration: while degradation of PCL/TCP scaffolds creates space for cellular infiltration and new bone in-growth, excessive degradation may lead to collapse of the scaffolds and a loss of integrity, which might limit the adhesion and proliferation of osteoblasts. In addition, massive release of degradation products may promote inflammation and a foreign body reaction [26,27].

The implantation of synthetic scaffolds in the site of bone defect causes immune responses and changes in immune microenvironment, which in turn influence the immunological regulation of bone repair. Immune cells, including neutrophils, lymphocytes, dendritic cells and macrophages, participate in the formation of a bone-immune microenvironment. Neutrophils appear around biomaterials implanted during the initial inflammatory period, and the macrophages become the primary cells present in the host-scaffold interactions [28]. Macrophages are highly heterogeneous and plastic immune cells. According to their surface markers and cell function, macrophages are usually classified as classically activated M1 subtypes and alternatively activated M2 subtypes. “Classically activated” M1 macrophages, which are known for production of pro-inflammatory cytokines, are indispensable in initiation of inflammation, cell recruitment and clearance of debris at the early stage of bone repair. M2 macrophages are primarily involved in the termination the inflammation and bone formation in the middle and late stage of bone repair. Therefore, M2 macrophages are also referred to “anti-inflammatory” or “pro-regenerative” macrophages [29]. With increasing understanding of the important role of macrophages in bone tissue engineering, many researchers focused on the development of smart immune environment responsive materials to modulate the polarization of macrophages and promote bone regeneration [30,31]. Variations in the chemical and physical properties of degradable scaffolds during scaffold degradation and bone tissue replacement may alter the surrounding immune responses and concomitant bone repair processes. Although degradation of bio-degradable materials has been recognized to have crucial effects on bone regeneration, the underlying mechanisms still remain unclear. This lack of knowledge is mainly due to the stable properties and extremely slow degradation rate of biodegradable bone repair materials and the absence of a stable and biconically accelerated model of polymer-based scaffold degradation *in vitro*.

In this study, we verified that PCL/ β -TCP scaffolds with varied compositions exert profoundly different effects on bone healing at each stage of degradation. Therefore, based on these interesting findings, we designed and prepared a dynamic bio-degradation device for PCL/TCP scaffolds based on related research on bio-resorbable magnesium [32]. Using this device, we carried out extensive experiments to investigate the dynamic physiochemical changes and consequent biological effects of degraded scaffolds at different stages of the bone healing process. (see Scheme 1)

2. Materials and methods

2.1. Scaffold preparation

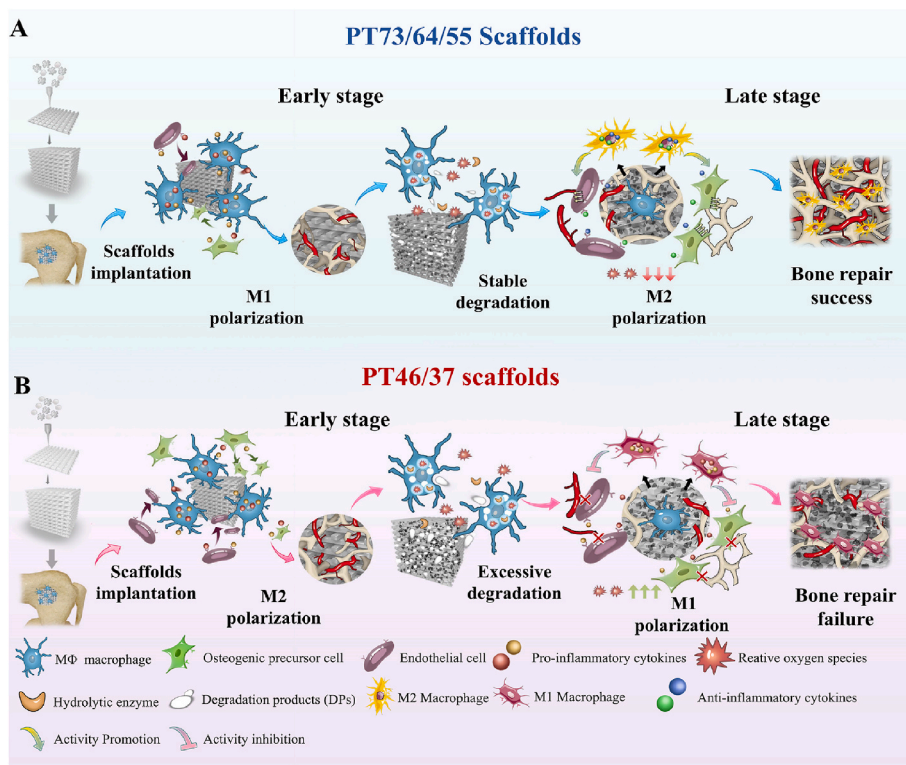
PCL/ β -TCP degradable scaffolds were fabricated using a fused deposition modeling technique, as previously reported. Medical grade PCL (Mn = 110 kDa) was purchased from PolyMTEK Biomedical Material Company (Shenzhen, China) and β -TCP was purchased from ZhongHong Chemical Co., Ltd (Lianyungang, China). The PCL and β -TCP were separately pulverized into granules at 60 °C and mixed at various PCL: β -TCP ratios (70:30, 60:40, 50:50, 40:60, and 30:70 by mass, designated as PT73, PT64, PT55, PT46 and PT37, respectively). The mixtures were added into a twin-screw melt extruder at 70 °C and the extruded mixtures were cut into rods with a diameter of 5 mm. The rods were then printed into three models of porous scaffolds (pore size: 600 μ m; filament diameter 400 μ m). Disc porous scaffolds (diameter 10 mm; height: 5 mm) were used for the *in vitro* cell experiments or subcutaneously implanted. Cylindrical porous scaffolds (diameter 3.5 mm; height 5 mm) were implanted into femoral defect zones. Cubic porous scaffolds (length of bottom edge 5 mm; height 10 mm) were used for the material characterizations and mechanical tests.

2.2. Scaffold characterization

Scanning electron microscopy (SEM, FE-SEM, S-4800, HITACHI, Japan) was used to assess the morphology of the scaffold surfaces. The crystal phases of the scaffolds were scanned by X-ray diffractometry (X Pert MPD PRO, PANalytical BV Netherlands) at a range of 10–90° at 8°/min under an operating voltage of 40 kV. The surface water contact angle of the PCL/TCP scaffolds was detected with a contact angle goniometer DSA100E (KRUSS, Germany). Fourier transform infrared spectra (FTIR) transmission spectra of PCL/TCP scaffolds were generated using a Spectrum FT-IR microscopy Nicolet IS5 (ThermoFisher, Waltham, MA, US) from 4000 to 500 cm^{-1} . Stress relaxation testing was performed using a Model 858 Material Testing System (MTS Systems, Eden Prairie, MN, USA) at 0.3 mm/min until 10% of maximum compressive strain was reached. Melting curves were generated by differential scanning calorimetry (DSC 3, Mettler-Toledo, Zurich, Switzerland). The viability of L-929 fibroblasts (Annoron, Beijing, China) was determined using the Cell Counting Kit-8 assay (CCK-8; Dojindo, Kumamoto, Japan) and adhesion morphologies of L929 fibroblasts seeded on scaffolds were assessed via SEM. MC3T3-E1 cells (bio-73319, Biobw, China) were cultured in scaffold-conditioned osteogenic media (Cyagen Biosciences, Inc., Santa Clara, CA, USA) and ALP activity was measured on day 5 using the Alkaline Phosphatase Color Development Kit (P0321, C3206, Beyotime Institute of Biotechnology) at an absorbance value of 410 nm. Alizarin red S (ARS, Sigma-Aldrich Co., St. Louis, MO, USA) staining was performed on day 10 to detect mineral nodules.

2.3. Dynamic bio-degradation model and characterization of degradation patterns

The novel biodegradation reactor shown in Fig. 2A was developed to characterize the PT scaffolds at different stages of degradation. The dynamic biodegradation reactor consists of a liquid peristaltic pump (flow speed: 0.007–7 mL/min; CHONRY, Baoding, China), a scaffold



Scheme 1. Schematic illustration of the mechanisms of scaffold degradation-mediated macrophage polarization and bone healing processes. A) Degradation of typical PT 55 scaffolds mediates sequential macrophage M1-M2 polarization and a matched “slow early-fast afterwards” bone regeneration mode. B) Degradation of typical PT37 scaffolds mediates ROS generation by macrophages, constant M1 polarization and a disordered “fast initially-slow in late stage” bone regeneration mode.

holder box (designed for fixation of cylindrical and cubic scaffolds), a peristaltic pump silicone tube (inner diameter: 0.8 mm, LONGER PUMP, Baoding, China) and a degradation medium container. Degradation media including hydrochloric acid (1 M), sodium hydroxide (1 M), lipase solution (100U/ml) and hydrogen peroxide were used to circulate in the biodegradation reactor. Hydrochloric acid and sodium hydroxide accelerate the hydrolysis of PCL/TCP scaffolds. Lipase is a type of hydrolytic enzyme, and the lipase solution accelerated the degradation of PCL/TCP through enzymatic hydrolysis. Oxidative degradation of hydrogen peroxide mainly depends on the attack of free radicals on the ester bonds. All scaffolds were fixed in the scaffold box, perfused with degradation medium (1 M sodium hydroxide). The degradation medium flow rate was set to 1 mL/min to mimic the flow of body fluids in bone tissue. The morphology of the materials, surface structure, mechanical properties, weight changes, molecular weights and degradation products were characterized after immersion of the scaffolds for 30, 60, 180 or 360 min. At the predetermined timepoints, the scaffolds were removed and dried for 3 h in a dryer. The morphology and compressive moduli of the degraded scaffolds were assessed as above described. The residue molecular weight was measured by gel permeation chromatography (Waters 1525, Milford, MA, USA). The dry weights of the scaffolds were recorded (Mn); M₀ was the initial scaffold weight. The percentage weight loss of the specimens was calculated using weight loss (%) = $(M_0 - M_n)/M_0 \times 100\%$. Finally, the degradation medium was collected and centrifuged. The degradation products were analyzed by transmission electron microscopy (TEM), electron diffraction and laser particle size analysis (LPSA). In brief, TEM (JEM-2100Plus, JEOL, Japan) at 300 kV was used to observe the morphology of the degradation particles, and the crystal structures of selected regions were determined by electron diffraction. The particle size of degradation products was analyzed by LPSA (Mastersizer 2000, Malvern Panalytical, UK).

2.4. In vivo bone repair experiments

All animal procedures were approved by the Institutional Animal Care Committee of Air Force Medical University. Male Sprague Dawley (SD) rats (12-weeks-old, weighing 280 ± 24 g) were acclimatized to a specific pathogen-free (SPF) environment. Sixty rats were divided into five groups, with twelve rats each. The animals were anesthetized using 4 mg/kg xylazine hydrochloride and 30 mg/kg of 2% (w/v) pentobarbital (Rongbai Biological Technology Co., Ltd, Shanghai, China) for surgery. Standardized cylindrical femoral defects (approximately 4 mm in diameter; 5 mm long internally and externally) were created in the distal femur above the medial femoral condyle under saline irrigation, then the defects were implanted with PT73, PT64, PT55, PT46 or PT37 cylindrical porous scaffolds. Bone wax was used to seal the tunnels and the wounds were sutured in layers. The rats received perioperative antibiotics (50 kU/kg penicillin) by intramuscular injection and post-operative medical care. Four rats in each group were sacrificed 4, 10 and 16 weeks after surgery.

2.5. Histological staining and immunohistochemistry

The rat femoral condyle specimens were cut into two parts for analysis ($n = 3$). For non-decalcified sections, the femur condyle samples implanted with the PT scaffolds were embedded in methyl-methacrylate (MMA) and 200- μ m-thick serial sections were prepared and polished to 50 μ m for fluorescent double-label analysis and Van Gieson staining. To achieve fluorescent double staining, rats were intramuscularly injected with alizarin red (75 mg/kg; Amresco Ltd., Boise, ID, USA) 14 days and calcein (8 mg/kg; Sigma-Aldrich) 4 days before euthanasia. Specimens were embedded in methyl-methacrylate (MMA), sectioned using a modified interlocked diamond saw (Leica Microtome, Heidelberg, Germany), and observed using a fluorescence microscope with a fluorescein

isothiocyanate (FITC) filter for alizarin red and rhodamine filter for calcein. The Bone formation rate/Bone surface (BFR/BS) of new bone formation was calculated as the distance between the two labels divided by time ($\mu\text{m}/\text{d} \times 100$; $n = 3$). For decalcified sections, the specimens were demineralized in 10% EDTA for 6 weeks and serial 5- μm -thick cross-sections were subjected to Masson's trichrome staining and TRAP staining (Sigma-Aldrich) according to the manufacturer's instruction. For immunohistochemical fluorescent staining, sections were incubated with specific primary antibodies overnight at 4 °C, including anti-CD68 (ab125212, Abcam, Cambridge, UK), Anti-CD206 (ab64693, Abcam) and Anti-CCR7 (ab32527, Abcam), followed by corresponding secondary antibodies (ab150080, ab150077 and ab150075, Abcam) and DAPI (ThermoFisher), and imaged using a fluorescent microscope (FV1000, Olympus, Japan).

2.6. Morphological observations

The femur samples ($n = 3$ per group) were dissected, fixed in 80% ethanol and subjected to micro-CT scanning (SKYSCAN 1276; Bruker, Germany). The region of interest (ROI) was a $3.5 \times 3.5 \times 5 \text{ mm}^3$ cylindrical region centered on the tunnel defect along the same major axis. The scanning parameters were a scan resolution of 8 μm , scan angle of 360° rotation, scan voltage of 80 kV and scan current of 500 μA . CT Analysis and VG Studio 2.1 software (Heidelberg, Germany) were used to analyze the data in 2D and 3D and VG Studio 2.1 software was used to analyze the bone volume and scaffold volume ratio. The ultra-microscopic morphological and elemental composition changes in the scaffolds implanted *in vivo* were characterized by scanning the scaffold-bone tissue interface using SEM and Energy EDS at a voltage of 15 kV. EMAX ENERGY (S-4800, HITACHI, Japan) was used to determine the chemical composition and content of the samples. Ca, P and O elemental signals were recorded and calculated.

2.7. *In vitro* co-culture of macrophages with degraded scaffolds

SEM and EDS inspection of degraded scaffolds *in vitro* were performed at regular intervals. The surface erosion and elemental composition were recorded. The Ca, P and C elemental signals *in vitro* were counted and relevant elemental contents were used to match that of scaffolds *in vivo* at 4, 10 and 16 weeks. The stage of degradation was classified as D1 (early stage), D2 (mid-stage), or D3 (late stage), which correspond to the stage of degradation *in vivo* at 4, 10, and 16 weeks. Specific elemental contents and the degradation time required for different scaffolds were recorded in Fig. S6 in supplementary material.

RAW 264.7 macrophages (icell-m047, iCell Bioscience Inc., Shanghai, China) were cultured in Dulbecco's modified Eagle's medium (HyClone, Logan, UT, USA) and 10% fetal bovine serum (FBS; Gibco, Waltham, MA, USA) in a 5% CO₂ atmosphere in an incubator at 37 °C; the medium was changed every day. All degraded scaffolds were washed with PBS for 24 h and sterilized with ethylene oxide, then 200 μL of RAW 264.7 macrophage suspension (5×10^4 cells/mL) was dropped on the different groups of degraded scaffolds ($n = 3$) and treated and analyzed as described below.

2.7.1. Morphological observation of macrophages on degraded scaffolds

Macrophage-scaffold composites were cultured in an incubator at 37 °C for 3 days, fixed with 3% *v/v* glutaraldehyde at 4 °C for 6 h, then dehydrated in a graded ethanol series, critical-point dried, sputtered with gold and subjected to SEM analysis.

2.7.2. Macrophage protein analysis

For immunofluorescent staining, RAW264.7 macrophages cultured with the degraded scaffolds for 48 h were fixed with 4% paraformaldehyde for 20 min, permeabilized with 0.2% Triton X-100 for 20 min, blocked with 1% bovine serum albumin for 2 h, and incubated with primary antibodies against CD86 (ab119857, Abcam) and CD206

(ab64693, Abcam) diluted 1:200 at 4 °C overnight. The composites were then incubated with Goat anti-Rat Alexa Fluor 647 conjugated secondary antibody (ab150167, Abcam) and Goat anti Rabbit Alexa Fluor 488 conjugated secondary antibody (ab15077, Abcam) for 1 h, followed by nuclear staining with 4,6-diamidino-2-phenylindole (DAPI) for 5 min.

For western blotting, the RAW264.7 macrophages cultured on the degraded scaffolds were lysed with RIPA Lysis and Extraction Buffer (ThermoFisher), the protein concentrations were determined using the BCA protein concentration assay kit (P0012S, Beyotime, Shanghai, China), 30 μg protein from each sample was subjected to electrophoresis (SDS-PAGE) and transferred to a polyvinylidene difluoride (PVDF) membrane (Merck Millipore, MA, USA). The membrane was blocked in 5% *w/v* bovine serum albumin (BSA, Solarbio, Beijing, China) and incubated with blocking buffer containing the diluted primary antibodies including Anti-iNOS antibody (13120S, Cell Signaling Technology, USA), Anti-liver Arginase (ab91279, Abcam) and anti-tubulin (ab6046, abcam) overnight at 4 °C. After incubation with Goat anti-Rabbit and Goat anti Mouse secondary antibody (H + L) HRP (SA-10011, SA10010, InCellGene, TX, USA) for 1 h, the protein bands were visualized using Western SuperSensitive substrate (IC-8001, InCellGene, TX, USA) and imaged using a ChemiDoc XRS System (BioRad, Hercules, CA, USA).

Enzyme Linked Immunosorbent Assay kits were used to determine the levels of IL-6 and TNF- α (70-EK282/4-96, 70-EK206/3-96, MULTISCIENCES (LIANKE) BIOTECH, CO., LTD, China) and IL-10 (SEA056Mu, Cloud-Clone Corp., Houston, TX, USA) in the supernatant of the culture media.

2.8. Subcutaneous implantation of degraded scaffolds

A subcutaneous scaffold implantation model was established in rats in order to evaluate the foreign body reaction and macrophage response to degraded scaffolds. In brief, fifteen female SD rats were anesthetized as previously described. Three areas on the back (located symmetrically along the spine) were shaved and disinfected with iodophor and three subcutaneous pockets were created by making 1-cm-long vertical incisions, and scaffolds at specific stages of degradation (D1-D3) were carefully inserted. The wounds were sutured and closed, and the rats received perioperative antibiotics (50 kU/kg penicillin) by intramuscular injection and post-operative medical care. The rats were euthanized 2 weeks after surgery and the samples were processed for H&E staining according to standard methods and immunohistochemical fluorescent staining of the macrophage-related surface markers CD68, CCR7 and CD206 was performed as previously described.

2.9. Immunoregulation of osteogenesis

To investigate the ability of macrophages to immunoregulate angiogenesis and osteogenesis in response to degraded scaffolds, RAW264.7 macrophages were incubated with PT scaffolds at different stages of degradation (D1-D3) in DMEM medium for 48 h, then the culture supernatants were collected in 1.5 mL microcentrifuge tubes. MC3T3-E1 osteoblast precursor cells cultured in the macrophage-conditioned media and subjected to ALP staining, Transwell assays and tube-forming experiments, as previously described.

2.10. RNA sequencing and data analysis

RAW264.7 macrophages were cultured with PT55 scaffolds and PT37 scaffolds at the mid-stage of degradation (PT55 D2 and PT37 D2), collected and total RNA was extracted using TRIzol reagent (Invitrogen, Carlsbad, CA, USA). Enrichment of mRNA, fragmentation, reverse transcription, library construction, HiSeq X Ten and data analysis were performed by Genergy Biotechnology Co. Ltd. (Shanghai, China). The thresholds for differentially expressed transcripts (DETs) were $P < 0.05$ and an absolute fold change ≥ 2 . DETs were subjected to function and

signaling pathway enrichment analysis using the GO and KEGG databases.

2.11. Phagocytic function of macrophages

The interactions and phagocytosis of degraded scaffolds by macrophages were directly observed by transmission electron microscopy. In brief, RAW264.7 macrophages were cultured with the degraded scaffolds for 48 h, collected, fixed with 2.5% glutaraldehyde, treated with 1% osmic acid fixative and dehydrated. The samples were embedded, sectioned and double-stained with uranyl acetate and lead citrate. The ultrathin sections were observed by TEM (HT7800, Hitachi, Japan). The macrophages were also labeled with Lyso-Tracker (C1046, Beyotime) for 1 h and observed by fluorescent microscopy at an excitation wavelength of 594 nm.

2.12. Analysis of oxidative stress in macrophages

The levels of oxidative stress-related proteins (Nox2 and Sod1) were analyzed by western blotting, as described above, using primary Anti-Nox2 (ab129068, Abcam), Anti-SOD1 (10269-1-AP, Proteintech, China) and anti-GAPDH (ab9485, abcam) antibodies.

To quantify the levels of reactive oxygen species (ROS), RAW264.7 macrophages were incubated with degraded PT scaffolds, then the cells were digested, collected, labeled with the fluorescent oxidation-sensitive probe 2',7'-dichlorodihydrofluorescein diacetate (DCFH-DA; Beyotime) and analyzed by flow cytometry (FACS Vantage SE; BD Biosciences, NJ, USA).

2.13. Inhibition of macrophage phagocytosis or endocytosis

To further investigate the role of macrophage phagocytosis in scaffold degradation-mediated immunoregulation, macrophages were cultured with PT37 scaffolds at the mid-stage of degradation (D2) in 12-well plates, pre-treated with 30 μM of the endocytosis inhibitors chlorpromazine (CPM, B1480; APExBIO, Houston, TX, USA) or 10 μM latrunculin B (Abcam) for 2 h, and then macrophage polarization were examined using immuno-fluorescent staining as described above.

2.14. Statistical analysis

Quantitative data are expressed as the mean ± standard deviations (SD) of at least three animals or three independent experiments. After confirming the data were normally distributed using the Kolmogorov-Smirnov test, the differences between groups were analyzed using one-way ANOVA or two-way ANOVA analysis of variance, followed by Dunnett's or Turkey's post hoc test. The levels of significance were set at *P < 0.05, **P < 0.01 and ***P < 0.001.

3. Results

3.1. Characterization of the physicochemical and osteogenic properties of 3D-printed PCL/β-TCP composite scaffolds

A series of bioactive PCL/TCP (PT) scaffolds with mass ratios ranging from 70/30 (PT73 group) to 30/70 (PT37 group) were prepared by FDM, as described in our previous studies (Fig. 1A, a1-a5). The porosity and surface morphology of the PT scaffolds were assessed by SEM and

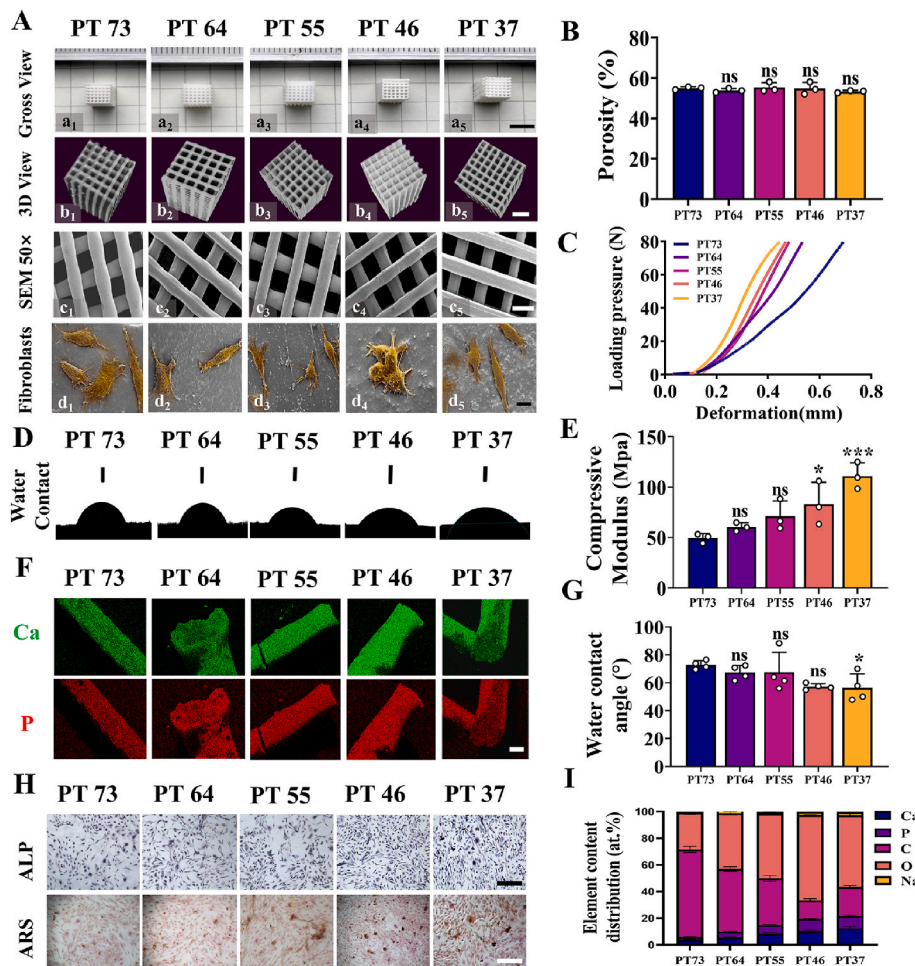


Fig. 1. Characterization of biodegradable PCL/β-TCP (PT) bone scaffolds with different mass ratios. A) a₁-a₅, Morphologic views of PT scaffolds prepared by FDM with mass ratios ranging from 70/30 (PT73) to 30/70 (PT37); scale bar: 5 mm; b₁-b₅, Micro-CT reconstructions of PT scaffolds; scale bar: 1 mm; c₁-c₅, Microstructure of cross-linked PT scaffolds observed by SEM; magnification, 1000 ×; d₁-d₅, Assessment of the biocompatibility of PT scaffolds towards L929 fibroblasts; scale bar: 20 μm. (B) Statistical analysis of scaffold porosity, n = 3. (C) Representative normalized compression-deformation curves of PT scaffolds. (D) Water contact angles of PT scaffolds. (E) Compressive moduli of PT scaffolds (n = 3). (F) Elemental distribution (Ca P) of sectioned PT scaffolds; scale bar: 100 μm. (G) Statistical analysis of the water contact angle of PT scaffolds, n = 4. (H) ALP staining and Alizarin red staining of osteogenesis in MC-3T3 osteoblasts cultured with PT scaffolds *in vitro*; scale bar = 200 μm. (I) Statistical analysis of the elemental compositions of sectioned PT scaffolds; n = 3. ns: not significant, *P < 0.05, **P < 0.01, and ***P < 0.001. vs. PT73 scaffolds, one-way ANOVA with Dunnett's post-hoc test.

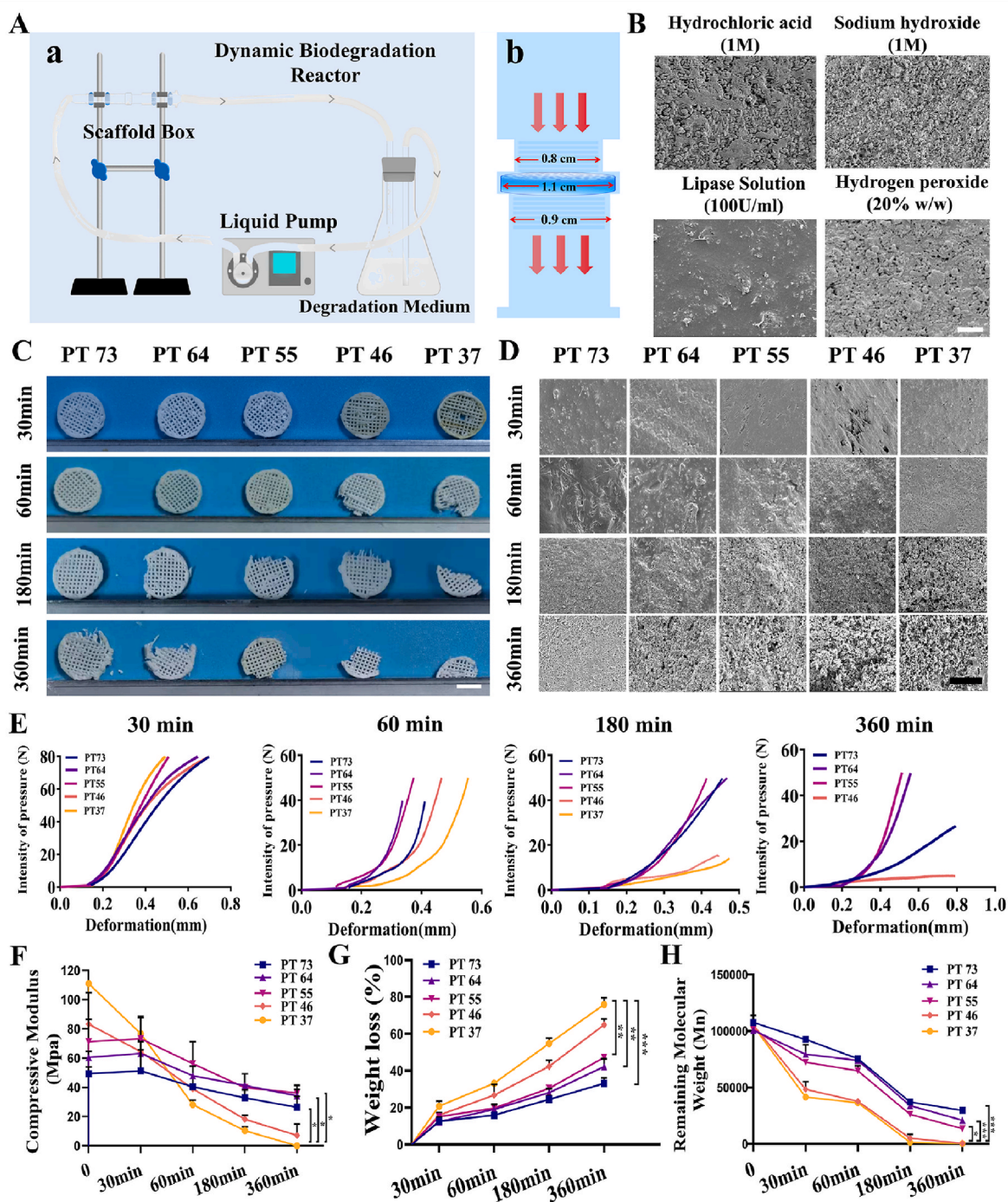


Fig. 2. Dynamic biodegradation of PT scaffolds *in vitro*. (A) a-b, Schematic illustration of the dynamic biodegradation reactor and degradation medium perfused through the PT scaffolds. (B) SEM analysis of the effects of degradation media including hydrochloric acid (180 min), sodium hydroxide (180 min), lipase solution (24 h) and hydrogen peroxide (24 h) on PT37 scaffolds, scale bar = 10 μm . Dilute sodium hydroxide was selected for the subsequent experiments. (C) Changes in the general appearance of PT scaffolds (scale bar = 5 mm) and (D) corresponding surface morphologies of PT scaffolds observed by SEM (scale bar = 10 μm) after 30–360 min degradation. (E) Typical compression-deformation curves of PT scaffolds after 30-, 60-, 180-, and 360-min degradation. (F–H) Dynamic changes in the compressive moduli, percentage weight loss and remaining molecular weight of PT scaffolds during 360-min degradation, $n = 3$. * $P < 0.05$, ** $P < 0.01$, and *** $P < 0.001$. vs. PT73 scaffolds, one-way ANOVA with Dunnett's post-hoc test.

micro-CT (Fig. 1A, b1-c5). Quantitative data revealed that all of the 3D-printed scaffolds had almost the same porosity (Fig. 1B). Biocompatibility assays confirmed that L929 fibroblasts adhered and spread well on the scaffolds (Fig. 1A, d1-d5).

Stress-strain curves generated by compressive testing showed the compressive moduli of the PT scaffolds increased with the proportion of TCP ceramic; the PT37 scaffolds exhibited the highest compressive

modulus of 110.9 ± 13.2 MPa (Fig. 1C and E). All of the scaffolds had hydrophilic surfaces, and the water contact angles decreased as the content of TCP ceramic increased (Fig. 1D and G). Crystal structures obtained by X-ray diffraction (XRD) revealed all PT scaffolds exhibited main polycaprolactone and $\text{Ca}_3(\text{PO}_4)_2$ peaks (Fig. S1A). In FTIR analysis (Fig. S1B), the characteristic peaks of PCL were observed at $2865\text{--}2952$ cm^{-1} (C–H stretching), $1723\text{--}1741$ cm^{-1} (C=O stretching) and 1160--

1190 cm^{-1} (C–O stretching), and the characteristic peaks of TCP ($\text{Ca}_3(\text{PO}_4)_2$) were observed at 1009–1041 cm^{-1} (P–O stretching) and 522–606 cm^{-1} (P–O bending).

The thermal properties of the PT scaffolds were characterized by differential scanning calorimetry (DSC). The melting temperature (T_m) of PCL was stable at approximately 60 °C, while the decomposition temperature (T_d) of PCL was approximately 410 °C (Fig. S1C). The elemental compositions of the PT scaffolds were analyzed by energy dispersive spectrometry (EDS). Elemental mapping and the profiles of sectioned scaffolds showed a uniform distributions of TCP particles (Fig. 1F). The elemental profiles and statistical analysis of Ca, P, C, O and other elements showed that the contents of Ca and P increased with the proportion of TCP; the percentage atomic weights of Ca and P in the PT37 scaffolds were $12.31 \pm 1.11\%$ and $9.22 \pm 0.71\%$, respectively (Fig. 1F and I).

The osteogenic effects of the 3D PCL/ β -TCP scaffolds towards MC-3T3 osteoblasts were verified by ALP and ARS (Fig. 1H). The scaffolds with higher TCP contents led to enhanced ALP activity, especially the PT37 scaffolds (Fig. S1D).

3.2. Construction of a dynamic degradation model to investigate scaffold biodegradation

To characterize the dynamic changes in the physicochemical properties and biological effects of biodegradable PCL/ β -TCP scaffolds at different stages during bone repair, we designed and developed an advanced dynamic biodegradation reactor to simulate the biodegradation environment *in vivo*. The flow rate of the reactor was set to 1 mL/min to mimic physiological tissue fluid movement (Fig. 2A, Fig. S2A). Cell culture medium (DMEM) or PBS led to minimal scaffold degradation after circulation in the reactor for 72 h (data not shown). Thus, we investigated the effects of several previously reported degradation media on PT scaffold degradation in the dynamic degradation reactor (Fig. 2B).

Dilute sodium hydroxide solution induced stable degradation patterns similar to the patterns of degradation observed for scaffolds implanted *in vivo* (Fig. 2B). Visual and SEM observations revealed the morphology and surface topography of the PT scaffolds gradually changed during the dynamic degradation process up to 360 min (Fig. 2C and D). The representative macro-scale images show the PT46 and PT37 scaffolds disintegrated after 60 min of degradation, and most of the PT46 and PT37 scaffolds were completely degraded after 360 min. Most of the degraded PT73, PT64 and PT55 scaffolds remained intact after 360 min degradation (Fig. 2C). The PT scaffolds exhibited an obviously corroded morphology after 180 min of the dynamic degradation process. The surfaces of PT73, PT64 and PT55 scaffolds appeared mildly corroded while the degraded PT46 and PT37 scaffolds seemed to have a rougher surface, with more abundant micro-holes and pits (Fig. 2D).

XRD, FTIR and DSC analysis of degraded scaffolds showed that the chemical phase, chemical groups and melting temperature of the PT46 and PT37 scaffolds were slightly altered after 60 min degradation (Fig. S2B, Fig. S2C). Moreover, the crystal phase, chemical bonding and melting curves of all PT scaffolds (except for PT73 scaffolds) were markedly changed after 360 min degradation (Fig. S2D, Fig. S2E).

The mechanical properties of the PT scaffolds were monitored by generating typical compression-deformation curves after 60–360 min degradation (Fig. 2E). The compressive moduli of all scaffolds progressively decreased during the 360-min degradation period. Notably, the mechanical properties of the PT73, PT64 and PT55 scaffolds were maintained after 360 min degradation, while the mechanical properties of the PT46 and PT37 scaffolds were completely lost (Fig. 2F). The PT73, PT64 and PT55 scaffolds exhibited two stages of loss of mechanical strength: a rapid loss during the initial 30 min and more gradual loss from 60 to 360 min. In contrast, the PT46 and PT37 scaffolds underwent constantly accelerating weight loss (Fig. 2G). The changes in the average molecular weight (Mw) of the degraded scaffolds are shown in Fig. 2H.

The molecular weight of the PT46 and PT37 scaffolds dropped sharply throughout the degradation process. Interestingly, there was a relatively stable stage of molecular weight in all PT scaffolds, which may be due to crystallization of the PT scaffolds (Fig. 2H).

Finally, micro-CT cross-sections of the *in vitro* degraded scaffolds confirmed the efficacy of the dynamic degradation reactor. Surface erosion and dense degradation products (DPs)-similar to those observed inside implanted PT scaffolds-were noted at 60 min during the *in vitro* biodegradation process (Fig. S2F). Reconstruction of the DPs by adjusting the μ -CT analysis threshold showed that DPs of varying sizes were uniformly distributed inside the scaffolds that were degraded *in vitro* (Fig. S2F).

3.3. Effects of PCL/ β -TCP scaffold composition on bone regeneration *in vivo*

As shown in the schematic illustration of the *in vivo* results (Fig. 3A), PT scaffolds with varied compositions led to two typical patterns of bone repair processes, and the rapid degradation of PT46/37 scaffolds caused bone failure at the late stage of bone repair. As shown in the representative micro-CT 3D reconstruction images, the PT73, PT64 and PT55 scaffolds underwent stable scaffold degradation and bone ingrowth, and the bone repair was successfully completed at 16 weeks. In contrast, despite inducing a relatively rapid bone in-growth rate at 4 weeks after implantation, the PT46 and PT37 scaffolds significantly hindered bone formation and led to an obvious reduction in the scaffold volume by 10 and 16 weeks (Fig. 3B).

Quantitative analysis confirmed a progressive increase in the ratio between the bone volume and total volume of the region of interest for the PT73, PT64 and PT55 scaffolds. Although the PT46 and PT37 scaffolds induced more new bone formation at 4 weeks than the other scaffolds, the volume of new bone barely increased further at 10 weeks and even decreased at 16 weeks (Fig. 3E).

Masson staining of the implanted zone confirmed the results obtained from the micro-CT reconstructions. As shown in Fig. 3C, though the area of new bone was obviously larger in the peripheral areas of the PT46 and PT37 scaffolds at 4 weeks, the bone ingrowth process in the PT46 and PT37 scaffolds was obviously disrupted scaffolds by 10 and 16 weeks.

Furthermore, a higher abundance of bone trabecular structures was observed inside the implanted PT55 scaffolds at 16 weeks (Fig. 3C and F). The rate of bone formation was measured by repeated injection of alizarin red and calcein for 10 days. Double fluorescence imaging revealed that the PT46 and PT37 scaffolds exhibited an abnormal pattern of bone regeneration: rapid bone neogenesis at 4 weeks and delayed bone formation at 10 and 16 weeks. The BFR/BS of the PT37 scaffolds was $2.00 \pm 0.14 \mu\text{m}^3/\text{d}^*100$ at 4 weeks and slowed to $0.27 \pm 0.02 \mu\text{m}^3/\text{d}^*100$ at 10 weeks and $0.29 \pm 0.03 \mu\text{m}^3/\text{d}^*100$ at 16 weeks. In contrast, osteogenesis gradually accelerated in the PT73, PT64 and especially the PT55 scaffolds over time (Fig. 3D). The BFR/BS of the PT55 scaffolds was $0.82 \pm 0.11 \mu\text{m}^3/\text{d}^*100$ at 4 weeks and increased to 1.83 ± 0.22 at 10 weeks and $2.01 \pm 0.11 \mu\text{m}^3/\text{d}^*100$ at 16 weeks (Fig. 3G).

3.4. Effects of PT scaffold degradation patterns on immunological responses and macrophage polarization

Based on the obvious rapid degradation of the PT46 and PT37 scaffolds observed in the micro-CT reconstructions, we further assessed the micro-topography of the sectioned bone-implant interfaces using SEM. Obvious erosion and higher numbers of cracks were detected on the surface of the sectioned PT46 and PT37 scaffolds than the other PT scaffolds. The PT73, PT64 and PT55 scaffolds were gradually enveloped by new bone tissues, from the peripheral zone to the center. In contrast, lamellar fibrous tissues were detected around the residual PT46 and PT37 scaffolds at 10 and 16 weeks (Fig. 4A). Micro-CT reconstruction

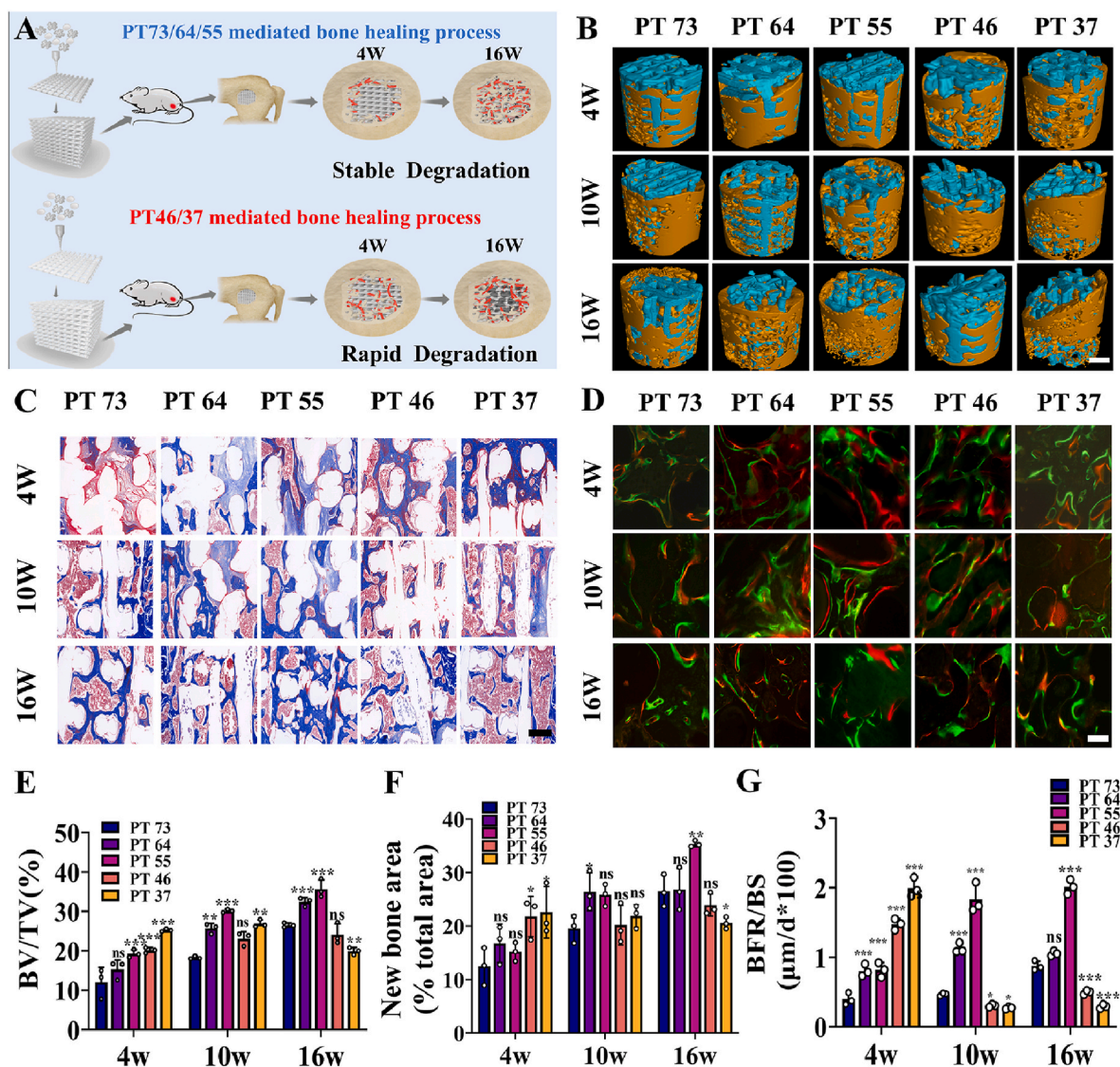


Fig. 3. (A) Schematic illustration of stable scaffold degradation and enhanced bone repair in the defects implanted with PT73, PT64 and PT55 scaffolds, and the rapid scaffold degradation and limited bone repair in defects implanted with PT46 and PT37 scaffolds. (B) Representative reconstructions of micro-CT images of implanted PT scaffolds (blue color) and bone in-growth (yellow color) at 4-, 10- and 16-weeks post-implantation; scale bar = 2 mm. (C) Representative Masson staining images showing new bone tissue around the PT scaffolds at 4-, 10- and 16-weeks post-implantation; scale bar = 100 μm . (D) Representative images of calcein/alizarin red labeling showing the rate of bone growth at 4-, 10- and 16-weeks post-implantation; scale bar = 100 μm . (E) Quantitative measurements of the new bone volume ratio (BV/TV) and residual material volume ratio (MV/TV) in the micro-CT region of interest (ROI) at 4-, 10- and 16-weeks post-implantation; $n = 3$. (F) Histological measurement of new bone area (%) at the implant site based on Masson staining, $n = 3$. (G) Bone formation rate/Bone surface, (BFR/BS) in the implant zone, $n = 3$. ns: not significant, * $P < 0.05$, ** $P < 0.01$ and *** $P < 0.001$. vs. PT73 scaffolds, two-way ANOVA with Dunnett's post-hoc test.

and segmentation of the residual scaffolds further confirmed the patterns of stable degradation of PT73, PT64 and PT55 scaffolds and rapid degradation of PT46 and PT37 scaffolds (Fig. 4B and E). Notably, high-magnification imaging of Masson-stained sections revealed a larger number of multi-nuclear giant cells (MNGCs) scattered over the scaffold zone of PT46 and PT37 scaffolds (Fig. 4C); TRAP staining demonstrated that these cells were distinct to multinuclear osteoclasts (Fig. S3A, Fig. S3C).

The observation of MNGCs inspired us to investigate the effects of the rapid degradation of PT46 and PT37 scaffolds on late stage in macrophage responses. Thus, as macrophage polarization is an important indicator of immunomodulation of the bone repair process, we performed tissue immunofluorescent staining to investigate the polarization of macrophages within PT scaffolds at different stages of the repair process. At 4 weeks, higher numbers of CD206+ M2 macrophages were observed in the PT46 and PT37 scaffolds, whereas higher numbers of CCR7+ M1

macrophages were found in the other PT scaffolds. Interestingly, the ratio of CD206+ macrophages decreased and CCR7+ M1 macrophages became dominant at 10 and 16 weeks in the defect zone of the PT46 and PT37 scaffolds. In contrast, a switch in polarization from CCR7+ M1 macrophages to CD206+ M2 macrophages was observed in the PT73, PT64, and PT55 scaffolds at 10 and 16 weeks (Fig. 4D, F, 4G). The M1-to-M2 macrophage switching of the PT73, PT64, and PT55 scaffolds is considered beneficial to bone repair, whereas the constant M1 polarization observed in the PT46 and PT37 groups may result in a failure of bone repair (Fig. 4F and G).

3.5. Matching the stages of degradation of PT scaffolds in vitro and in vivo

We investigated the degraded surface morphology and corresponding elemental distribution of the scaffolds at 4-, 10- and 16-weeks post-

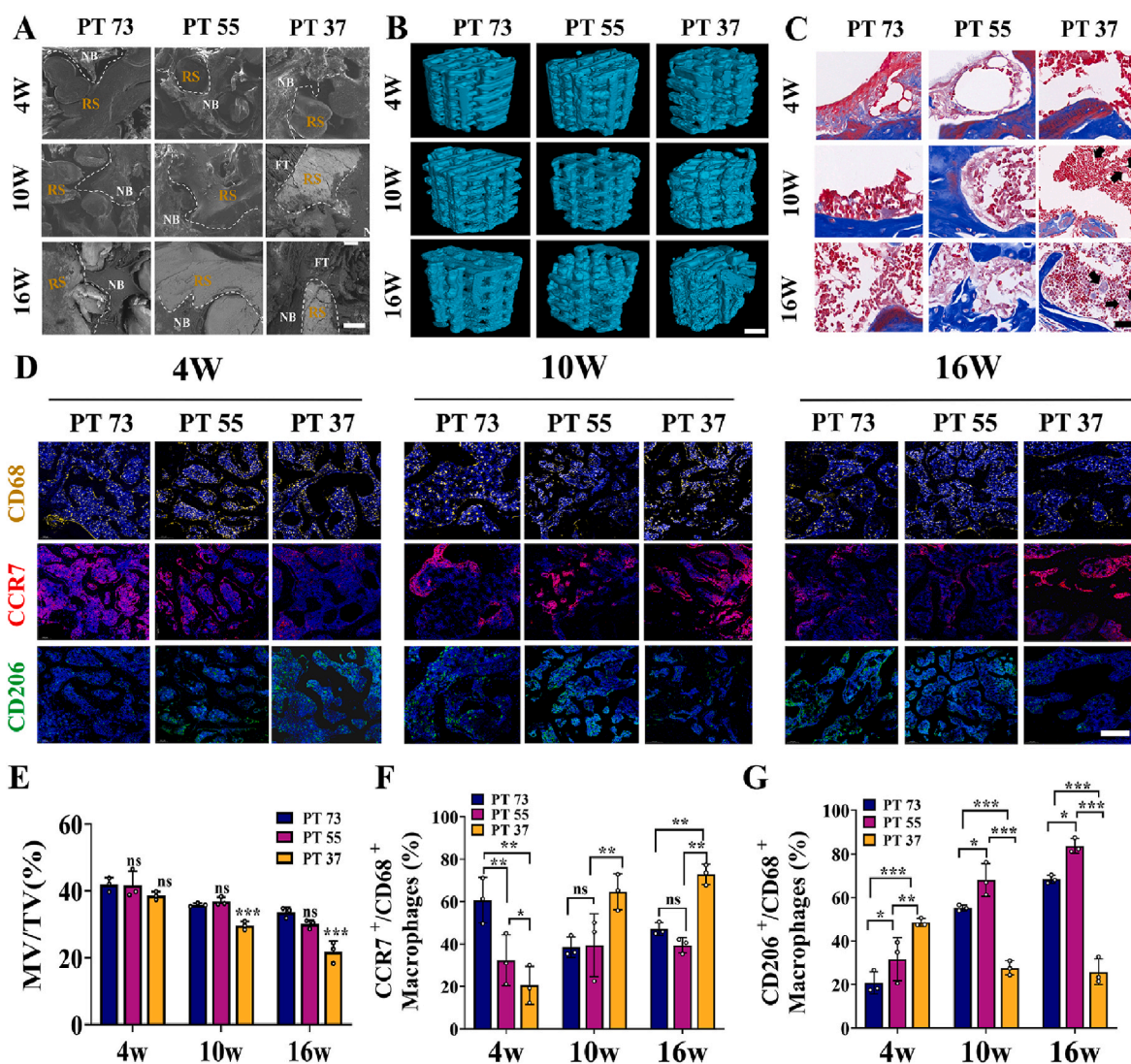


Fig. 4. Modes of scaffold degradation and immunological responses to PT scaffolds. (A) SEM analysis of the morphological changes during scaffold degradation and bone ingrowth at the implant-bone interface in defects implanted with PT73, PT55 and PT37 scaffolds at 4-, 10- and 16-weeks post-implantation; scale bar = 50 μ m. (B) Segmentation of the degraded scaffolds in the micro-CT reconstructions of the defect zones at 4-, 10- and 16-weeks post-implantation, scale bar = 2 mm. (C) Representative images of multi-nuclear giant cells (MNGCs, black arrow) inside the defect zone at 10- and 16-weeks post-implantation of PT37 scaffolds; scale bar = 20 μ m. (D) Representative immunofluorescence images of CD68+ macrophages and CCR7+ M1 and CD206+ M2 polarization in the defect zone at 4, 10 and 16 weeks; scale bar = 100 μ m. (E) Quantitative measurements of the residual material volume ratio (MV/TV) in the micro-CT region of interest (ROI) at 4-, 10- and 16-weeks post-implantation; n = 3. (F) Semi-quantitative analysis of the ratio of CCR7+/CD68+ cells; n = 3. (G) Semi-quantitative analysis of the ratio of CD206+/CD68+ cells; n = 3. ns: not significant, *P < 0.05, ** P < 0.01, and *** P < 0.001 vs. PT73 scaffolds, two-way ANOVA with Dunnett's post-hoc test.

implantation *in vivo* by SEM-EDS (Fig. 5A). The changes in the elemental compositions and degradation of PT scaffolds *in vivo* after 4, 10, and 16 weeks corresponded to early stage (D1), mid-stage (D2), and late stage (D3) degradation *in vitro*, respectively (Fig. 5B). The corresponding elemental compositions of Ca, P and C of scaffolds at each stage of degradation *in vitro* and *in vivo* are shown in Fig. 5C; the average atomic percentages and degradation time required for each scaffold are summarized in Fig. S4A. Micro-CT cross sections at 10 weeks showed surface erosion and dense degradation products (DPs) generated inside the implanted PT scaffolds during the *in vivo* biodegradation process (Fig. S4B).

3.6. Macrophage polarization switching at different stages of PT scaffold degradation *in vitro*

As shown in Fig. 6A, RAW264.7 macrophages were co-cultured with scaffolds at different stages of degradation to investigate the biological

effects of scaffold degradation on macrophage polarization and cytokine secretion. Remarkably, two distinct macrophage morphologies were observed on the surface of degraded scaffolds. Macrophages cultured with PT73 scaffolds at the D1 stage appeared as large round cells with abundant pseudopods, which is characteristic of M1 polarized macrophages. In contrast, macrophages on PT37 scaffolds at the D1 stage exhibited a flattened, elongated spindle-like shape, characteristic of M2 polarized macrophages. The phenotype of macrophages clearly switched with the stage of scaffold degradation from D1 to D3 (Fig. 6B).

To further explore the effects of scaffold degradation on macrophage polarization *in vitro*, RAW264.7 macrophages cultured with PT73, PT55 and PT37 scaffolds at different stages of degradation were subjected to immunofluorescent staining for CD86 and CD206 (Fig. S6A). The M1 marker CD86 was expressed at higher levels in macrophages on the PT73 scaffold than all the other scaffolds at the D1 stage, and CD86 expression level decreased at the D2 and D3 stages. In addition, expression of the M2 marker CD206 by macrophages on PT73 scaffolds

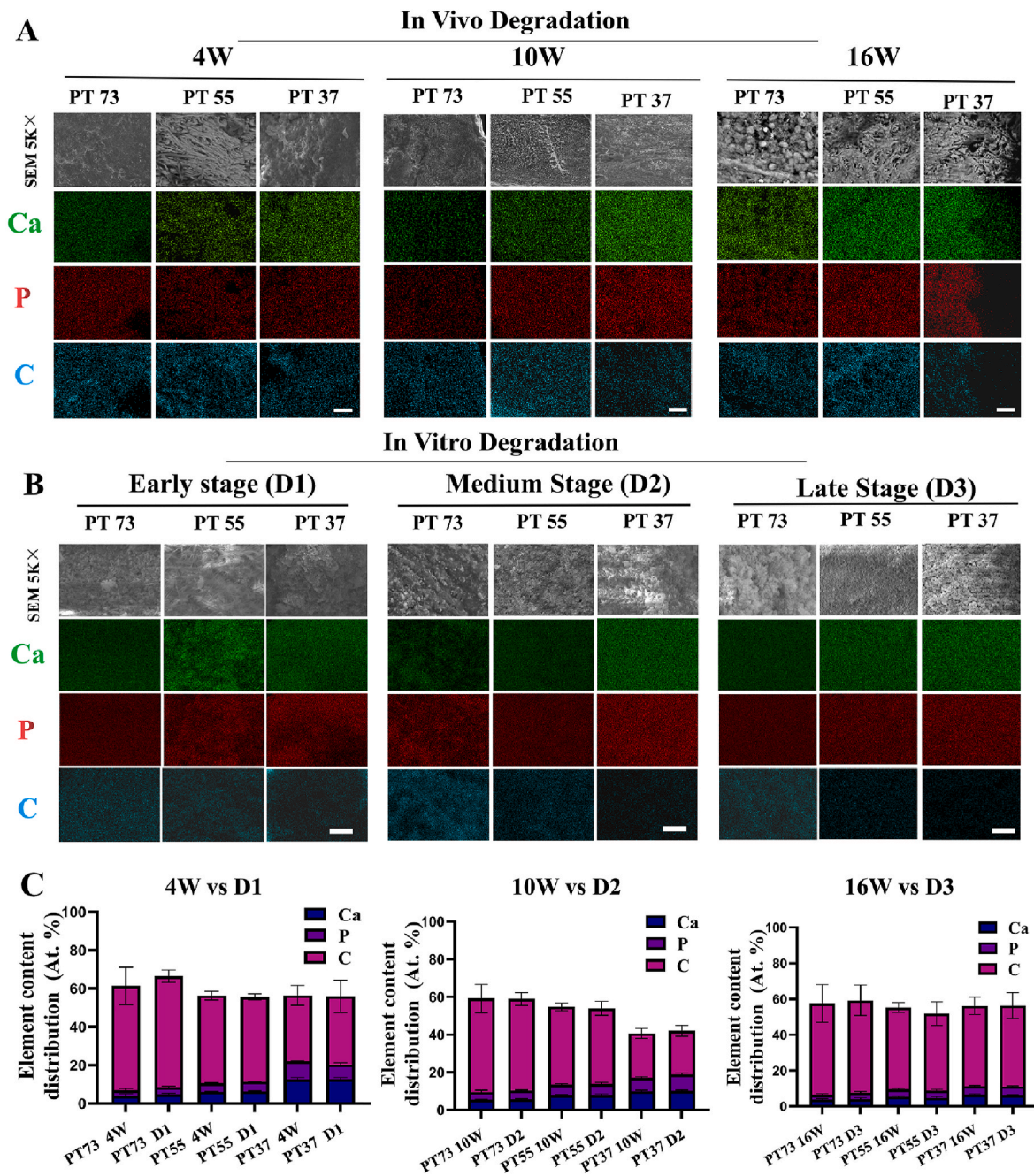


Fig. 5. Matching the stages of degradation of PT scaffolds *in vitro* and *in vivo*. (A) Morphological observation and elemental distribution mappings of PT scaffolds at 4, 10 and 16 weeks; scale bar = 10 μm. (B) Determination of scaffolds in the early degradation stage (D1), mid-degradation stage (D2) and late degradation stage (D3) based on SEM observations and EDS analysis of elemental distribution; scale bar = 10 μm. (C) Matching scaffolds degraded *in vivo* at 4, 10 and 16 weeks with *in vitro* degraded scaffolds at the D1, D2 and D3 stage based on statistical analysis of their elemental compositions, n = 3.

increased from the D1 to D3 stage. Macrophages cultured with PT55 scaffolds exhibited similar changes as macrophages cultured with PT73 scaffolds and CD206 expression was the highest in the PT55 groups at the D2 and D3 stages compared to other groups. However, although CD206 was highly expressed by macrophages on PT37 scaffolds at the D1 stage, CD206 expression obviously decreased at the D2 and D3 stages, accompanied by an increase in CD86 expression (Fig. 6C).

Next, we examined the protein expression of iNOS (an M1 marker) and arginase-1 (Arg-1, an M2 marker) in macrophages cultured with degraded scaffolds at the D1 to D3 stages. In addition, macrophages were treated with LPS or IL-4 to induce M1 and M2 macrophage polarization as positive controls. iNOS expression obviously increased in

PT37 scaffolds but was undetectable in macrophages cultured on PT55 scaffolds at the D2 and D3 stages (Fig. 6D).

As positive controls, LPS markedly increased the release of TNF-α and IL-6, while IL-4 efficiently stimulated the secretion of IL-10. Compared to macrophages on PT37 scaffolds at the same stages, macrophages cultured on PT73 and PT55 scaffolds secreted more IL-6 and TNF-α at the D1 stage, less IL-6 and TNF-α at the D2 and D3 stages, and higher levels of the anti-inflammatory cytokine IL-10 at the D2 and D3 stages. Macrophages cultured on PT37 scaffolds at the D2 and D3 stages secreted higher levels of pro-inflammatory IL-6 and TNF-α compared to cells on PT73 and PT55 scaffolds at the same stage (Fig. 6E–G).

The effects of macrophage-conditioned media (CM) on osteogenesis

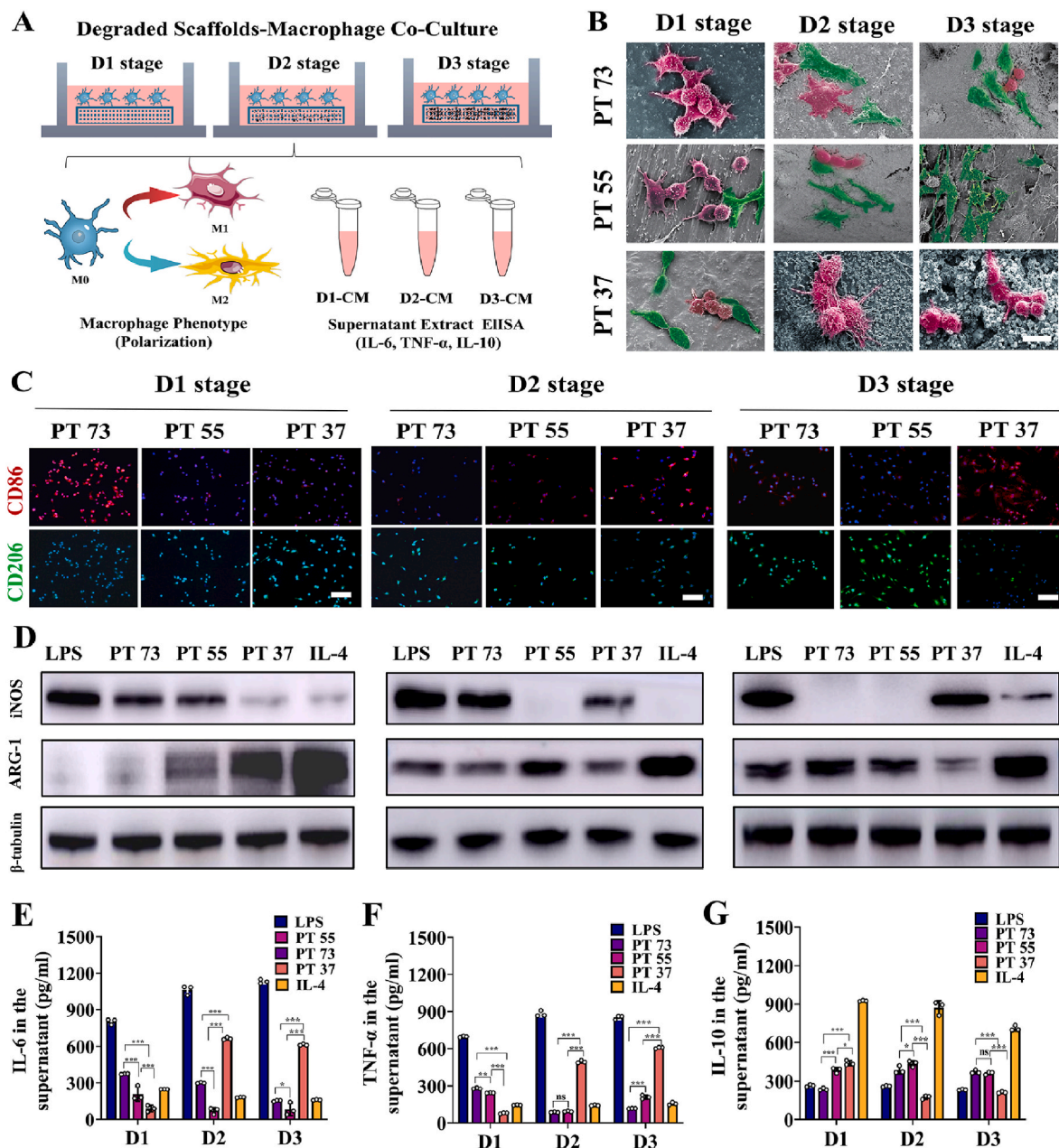


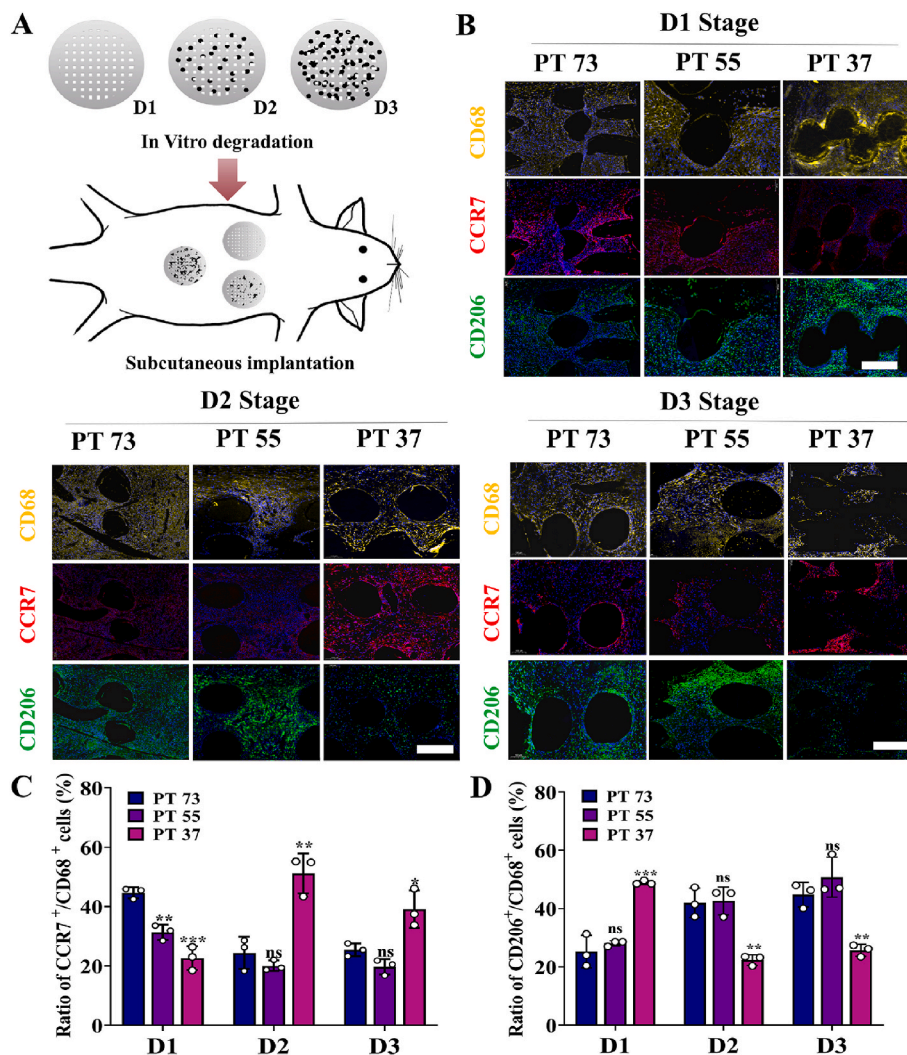
Fig. 6. Scaffold degradation induces dynamic processes of macrophage polarization. (A) Schematic illustration of the effects of scaffolds at different stages of degradation on macrophage polarization and cytokine secretion. (B) BIOSEM analysis of the morphological changes in macrophages on the surface of PT73, PT55 and PT37 scaffolds at the D1–D3 stages; scale bar = 10 μ m. (C) Representative immunofluorescent analysis of CD86 and CD206 expression (scale bar = 100 μ m) and (D) Western blot analysis of the expression of the M1 macrophage marker iNOS and the M2 macrophage marker Arginase-1 in RAW264.7 macrophages cultured with degraded scaffolds at the D1–D3 stages. (E–G) ELISAs of the levels of the proinflammatory cytokines TNF- α and IL-6 and the anti-inflammatory cytokines IL-10 in RAW264.7 macrophages cultured with degraded scaffolds at the D1–D3 stages, $n = 3$. ns: not significant, * $P < 0.05$, ** $P < 0.01$, and *** $P < 0.001$, two-way ANOVA with Turkey's post-hoc test.

were investigated using the ALP activity assays (Fig. S5B, Fig. S5C). CM from macrophages cultured with PT37 scaffolds at the D2 and D3 stages drastically inhibited osteoblast ALP activity, whereas CM from PT73 and PT55 scaffolds at the D2 and D3 stages significantly enhanced ALP activity (Fig. S5D).

3.7. Effects of the stage of PT scaffold degradation on macrophage polarization in vivo

As shown in Fig. 7A, biodegradable PT73, PT55 and PT37 scaffolds were pre-degraded to the corresponding D1, D2 and D3 stages *in vitro* and then implanted subcutaneously in the rat model. Interestingly, a

number of multinuclear giant cells (MNGCs) were found in the fibrous tissues with disordered collagen surrounding D2 stage PT37 scaffolds (Figs. S6A and S6B). The distribution and polarization of macrophages inside the PT scaffolds was investigated using immunofluorescent staining. Unlike the regional distribution of macrophages observed in PT scaffolds during bone repair, CD68⁺ macrophages were widely distributed inside the PT scaffolds subcutaneously implanted at different stages of degradation. Notably, consistent with the patterns of macrophage switching observed *in vitro* (Fig. 6C) CCR7⁺ M1 and CD206⁺ M2 macrophage polarization switching was observed in the bone scaffolds (Fig. 7B). The ratio of CCR7⁺/CD68⁺ macrophages decreased and the



ratio of CD206⁺/CD68⁺ macrophages increased in PT73 and PT55 scaffolds between the D1 to D3 stages. In addition, the number of CCR7⁺ M1 macrophages on PT37 scaffolds significantly increased at the D2 and D3 stages (Fig. 7C and D).

3.8. RNA-seq verification of the effects of PT scaffolds at the D2 stage of degradation on macrophage polarization

Based on the results above, we tentatively reasoned that the stage of degradation of PT scaffolds influences macrophage polarization and immunoregulation. To better understand the biological effects of degraded scaffolds on macrophage polarization, we carried out RNA sequencing (RNA-seq) to analyze gene expression in macrophages cultured *in vitro* with PT55 and PT37 scaffolds at the D2 stage of degradation.

In total, 1288 genes were upregulated, and 215 genes were downregulated in the PT37 D2 group compared with the PT55 D2 group (Fig. 8A and B). GO enrichment and network analysis showed that the terms immune response, defense response, response to external stimulus functions and acute inflammatory response were significantly upregulated in the PT37 D2 group. These functional annotations revealed that PT37 scaffolds at the D2 stage induced an intense immune response and an acute inflammatory response in macrophages compared to PT55 scaffolds at the D2 stage (Fig. 8C and E). KEGG analysis of DEGs in the PT37 D2 scaffold vs. PT55 D2 scaffold groups revealed enrichment of genes involved in the immune system, infectious diseases and signaling

molecules and interaction pathways; the TNF signaling pathway, NF-kappa B signaling pathway and allograft rejection pathways were significantly upregulated (Fig. 8D and F). Notably, the phagosome pathway was also among the top upregulated pathways in the PT37 D2 group, which indicates that phagocytic function and the phagosome pathway might contribute to the polarization of macrophages cultured with PT scaffolds.

3.9. Effects of degradation product phagocytosis and phagosome formation on macrophage oxidative stress and polarization

The KEGG pathway enrichment indicated that phagocytic function and phagosome pathways may play an important role in the macrophage responses to degraded scaffolds. Degradation products (DPs) in phagosomes are transported to lysosomes and digested by acid hydrolases. Thus, we used LysoTracker Red to label the lysosomes in macrophages cultured with scaffolds at the D2 stage of degradation and observed the cells by fluorescence microscopy (Fig. 9A). The numbers and fluorescence intensity of lysosomes were higher in the PT37 group compared to other scaffold groups, and the agglomeration of some of the lysosomes in the macrophages cultured on PT37 D2 scaffolds were observed (Fig. 9B). TEM showed that the DPs of the PT scaffolds had irregular shapes and uneven textures. Moreover, the heterogeneous DPs were semicrystalline, with a mixture of crystal zones and amorphous zones, as confirmed by electron diffraction (Fig. S7A). LPSA revealed that the DPs of PT37 scaffolds were larger than the DPs of the other

Fig. 7. Tissue immune responses to subcutaneously implanted degraded scaffolds. (A) Schematic illustration of the effects of subcutaneously implanted scaffolds at different stages of degradation on tissue immune responses in a rat model. (B) Representative immunofluorescence images of CD68⁺ macrophages and CCR7⁺ M1 and CD206⁺ M2 polarization in the defect zone for scaffolds at different stages of degradation; scale bar = 100 μm. (C) Semiquantitative analysis of the ratio of CCR7⁺/CD68⁺ cells, *n* = 3. (D) Semiquantitative analysis of the ratio of CD206⁺/CD68⁺ cells, *n* = 3.

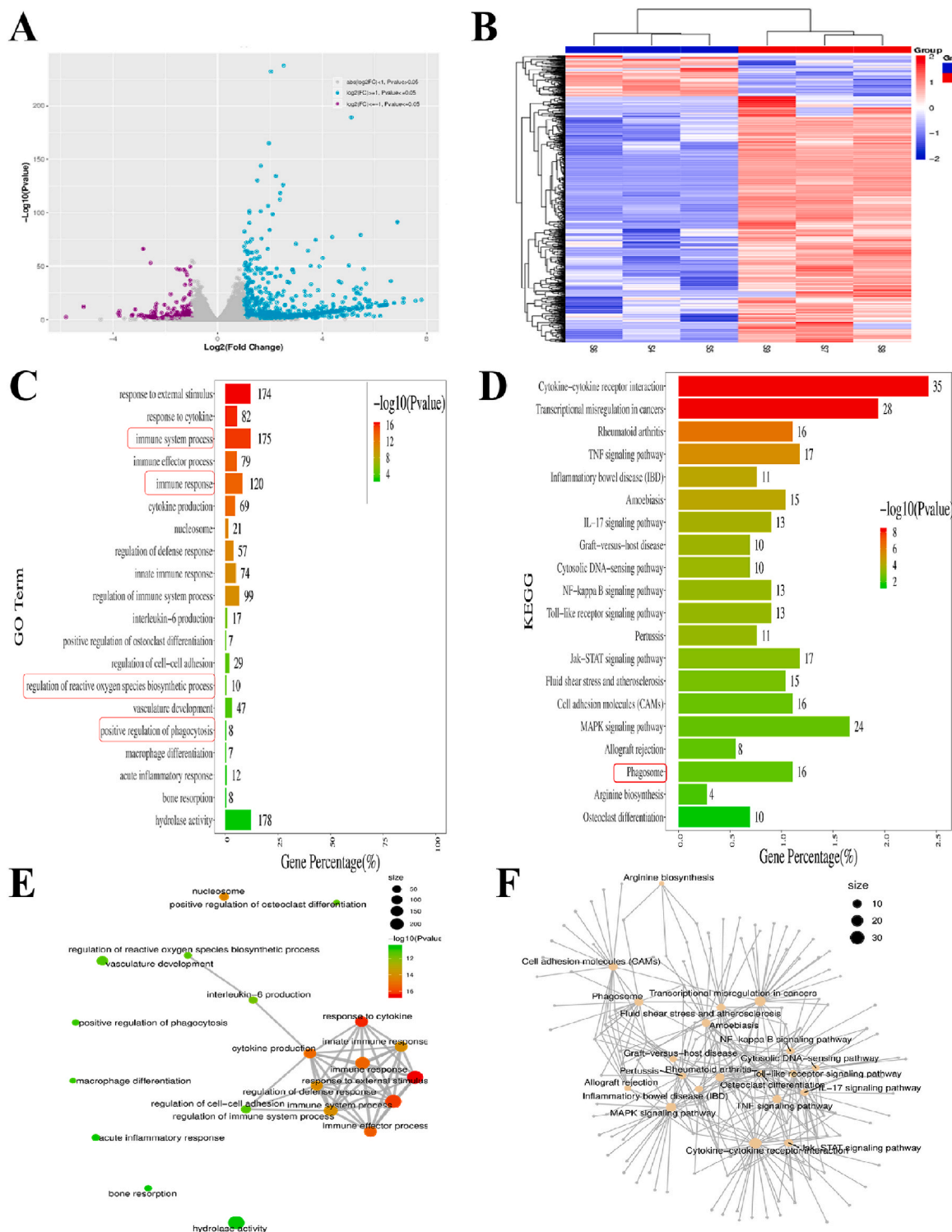


Fig. 8. RNA-seq analysis of macrophages cultured with degraded PT55 VS PT37 scaffolds *in vitro*. (A–B) Volcano plot, (B) heatmap diagram, (C) GO pathway enrichment, (D) KEGG pathway classification, (E) interaction network analysis and (F) candidate gene interaction network analysis of differentially expressed genes (DEGs) in macrophages in the D2 PT55 scaffold vs. D2 PT37 scaffold groups. ns: not significant, * $P < 0.05$, ** $P < 0.01$, and *** $P < 0.001$ vs. PT37 D2 group, one-way or two-way ANOVA with Dunnett’s post-hoc test.

scaffolds; some of the DPs in the PT37 group had diameters larger than 10 μm (Fig. S7B).

Next, the phagocytosis of DPs was directly visualized by TEM. A jumble of microcrystals was observed in the phagosomes of the macrophages, and these patterns were highly similar to the DPs observed *in vitro* (Fig. 9C, Fig. S7A). The DPs were integrated into the phagosome

and disintegrated into coarse particles, which varied greatly in size and components between scaffolds. The phagosomes in macrophages cultured with PT37 scaffolds at the D2 stage were significantly larger than the phagosomes in macrophages cultured with other PT scaffolds (Fig. 9D).

The potential influence of phagocytosed DPs on oxidative stress and

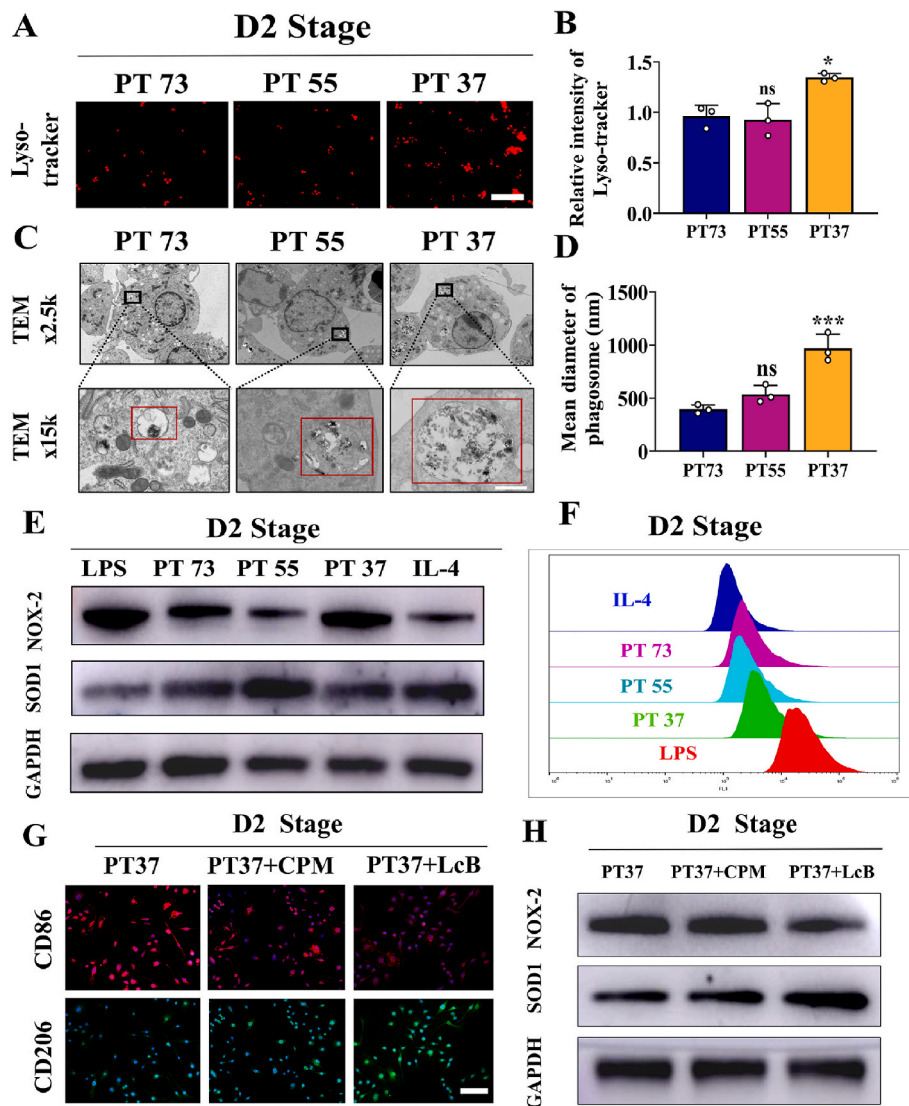


Fig. 9. Degraded PT37 scaffolds induce oxidative stress and polarization changes in macrophages. (A) Macrophages were cultured with scaffolds at the D2 stage of degradation for 24 h and lysosomes were labeled with LysoTracker (red); scale bar = 100 μ m. (B) Quantitation of the relative fluorescence intensity of LysoTracker in (A), $n = 3$. (C) TEM analysis of macrophage phagocytosis of the degradation products (DPs) of scaffolds at the D2 stage. The black boxes in the upper panel indicate the DPs and phagosome formation; scale bar = 500 nm. (D) Quantitative calculation of the mean diameter of phagosomes in (C); $n = 3$. (E) Western blotting of NOX-2, SOD and GAPDH protein expression in macrophages cultured with scaffolds at the D2 stages of degradation. (F) Representative flow cytometry analysis intracellular reactive oxygen species intensity of macrophages cultured with scaffolds at D2 stage of degradation. (G) Representative immunofluorescence images of CD86 and CD206 expression in RAW264.7 macrophages cultured with PT37 scaffolds at the D2 stage of degradation; cells were pretreated with or without chlorpromazine or latrunculin B before co-culture, scale bar = 100 μ m. (H) Western blot analysis of NOX-2 and SOD in RAW264.7 macrophages cultured with PT37 scaffolds at the D2 stage of degradation and pretreated with chlorpromazine or latrunculin B before coculture.

inflammation in macrophages were also studied. Western blot analysis showed that the PT37 scaffolds at D2 stage significantly promoted expression of the ROS-producing enzyme NOX2 and inhibited expression of the ROS-eliminating enzyme SOD1 (Fig. 9E). Flow cytometric analysis confirmed that the culture with PT37 scaffolds at the D2 stage induced higher production of ROS in macrophages than the other scaffolds (Fig. 9F).

To further determine whether the reactive stress and M1 polarization observed in macrophages were induced by the DPs of PT37 scaffolds at the D2 stage, we pretreated macrophages with chlorpromazine (CPM, an endocytosis inhibitor) or latrunculin B (LcB, a phagocytosis inhibitor) for 2 h. Immunofluorescent staining for CD86 and CD206 revealed that inhibition of phagocytosis by LcB obviously alleviated M1 polarization of macrophages cultured with PT37 scaffolds at the D2 stage (Fig. 9G). Western blot analysis showed that pretreatment with CPM and LcB, especially LcB, reduced the expression of NOX-2 in macrophages cultured with PT37 scaffolds at the D2 stage (Fig. 9H).

4. Discussion

PCL/ β -TCP bioresorbable bone repair scaffolds (PT scaffolds) with a range of compositions (70/30 to 30/70 w/w) were successfully constructed through FDM. The pore sizes of PT scaffolds were 422 ± 10 μ m and current studies have shown that the large macropores (greater than

250 μ m in diameter) promote osteogenic differentiation, vascularization and bone repair [33]. All of the scaffolds exhibited uniform porous structures and almost similar pore sizes and porosity. PT37 (30/70 w/w) scaffolds with the highest ceramic content were strongly hydrophilic and had the highest compressive strength. Consistent with previous studies, the PT37 scaffolds led to significantly improved osteogenic differentiation of MC-3T3 osteoblast compared to the other PT scaffolds [20,21].

Biodegradation of the PCL/TCP scaffolds was carried using a dynamic degradation reactor. *In vivo*, the degradation of PCL-based materials occurs in at least two stages: the first stage involves random hydrolysis of ester bonds and is associated with molecular weight loss, and the second stage involves bulk degradation when the molecular weight is less than 5000 [34,35]. During the degradation process, tissue enzymes (including lipase, esterase and proteases) and ROS (including hydrogen peroxide, nitric oxide and hydroxyl radicals) accelerate the hydrolysis and oxidation of metal and polymer scaffolds [36–38]. Based on these previous reports of the characteristics of accelerated degradation, we examined the effects of various degradation media, including hydrogen peroxide, lipase, sodium hydroxide and hydrochloric acid solution, on scaffold degradation *in vitro* [38–40]. *In vivo*, the flow of tissue fluid influences also the degradation rate as accumulation of DPs in a static environment *in vitro* may limit further degradation. Thus, we manufactured a biodegradation reactor with a peristaltic pump and

controlled the liquid circulation at 1 mL/min to mimic physiological tissue fluid movement [32,41,42].

Within a reasonable time, PT scaffolds degraded in the reactor by circulation with diluted sodium hydroxide exhibited analogous degradation patterns to scaffolds implanted *in vivo*. The dynamic degradation reactor enabled us to monitor the changes in the physiochemical properties of the scaffolds throughout the degradation process. The PT46 and PT37 scaffolds degraded rapidly in the degradation reactor and exhibited obviously corroded surfaces at the end of degradation. Although the PT46 and PT37 scaffolds retained high compressive strength after 30 and 60 min of degradation, their mechanical strength quickly decreased and was almost completely lost after 180 min. In contrast, the PT73 to PT55 scaffolds maintained high mechanical strength after 360 min of *in vitro* degradation. Weight loss and molecular weight change curves confirmed that the PT46 and PT37 scaffolds changed significantly and lost their integrity during degradation.

Though the PT46 and PT37 scaffolds exhibited better mechanical strength and osteogenic ability *in vitro*, *in vivo* bone repair experiments demonstrated that the rapid degradation of PT46 and PT37 scaffolds negatively affected the bone formation process and lead to a failure of bone healing at 16 weeks. Despite promoting more new bone formation in the early stage, the PT46 and PT37 scaffolds subsequently impeded bone repair and remodeling. In contrast, the PT73, PT64 and PT55 scaffolds successfully induced bone ingrowth and bone regeneration. Micro-CT analysis revealed that the PT37 scaffolds degraded relatively rapidly and that the residual scaffolds were partially disintegrated at 16 weeks. SEM of the scaffold-bone interface revealed serious erosion of the surface of the PT37 scaffolds, in agreement with previous suggestions that the interface between implants and newly formed bone during degradation influence the bio-adaptation and repair effects of degradable scaffolds [43]. Masson staining revealed the existence of MNGCs around the residual scaffolds at 10 weeks and 16 weeks after implantation; these cells are typically distinct from TRAP + osteoclasts and highly associated with chronic inflammation and formation of a fibrous capsule [44,45]. Thus, we inferred that the rate of degradation of PCL/TCP scaffolds may interfere with immune responses and subsequently influence the immunoregulatory process that govern bone regeneration.

As the main primary effector cells of the immune system, monocyte macrophages play an indispensable role in modulating foreign body reaction (FBR) and inflammatory responses, including macrophage polarization in response to implanted biomaterials [46]. Macrophages exhibit functional plasticity and are highly affected by physiochemical changes, including changes in the mechanical strength, surface topography and chemical compositions of biodegradable scaffolds [47,48]. More importantly, a growing body of research has shown that sequential activation of heterogeneous macrophage phenotypes is essential for successful implant-induced bone repair [49–51]. Our immunological staining also revealed that the polarization state of macrophages changes over time during the bone healing process. In defects implanted with the PT73, PT64 and PT55 scaffolds, proinflammatory M1 macrophages dominated in the early stages and then decreased rapidly as macrophages polarized to an alternative M2 state. In contrast, sequential polarization from M1 to M2 was interrupted by PT46 and PT37 scaffolds, and sustained activation of M1 macrophages was observed. Thus, based on our finding, we conservatively speculated that the degradation of PT scaffolds affects macrophage polarization and determines the success of bone healing.

Although some studies have shown that the biodegradability, degradation rate and DPs of biomaterials all influence peri-implant macrophage function and responses [52–54], the biological effects of the scaffold degradation process on macrophage responses are poorly understood. The main factor for this knowledge gap is the difficulty of determining the specific stage of degradation of scaffolds *in vitro*. To overcome this issue, we degraded the PCL/TCP scaffolds *in vitro* using the dynamic degradation reactor and determined the corresponding

early stage (D1), mid-stage (D2) and late (D3) stage of degradation by matching the elemental distribution contents to scaffolds degraded *in vivo* [43], which allowed us to investigate the responses of macrophages to different patterns and stages of PT scaffold degradation.

SEM revealed macrophages incubated with various degraded scaffolds exhibited different shapes that are closely related to their polarization and function [55]. Immunofluorescence staining and western blotting further indicated that the large and round macrophages expressed high levels the M1 macrophage marker, while the elongated spindle-like macrophages tended to be M2 macrophages. ELISA of the levels of pro-inflammatory IL-6 and TNF- α and anti-inflammatory IL-10 demonstrated that degraded PT37 scaffolds promoted pro-inflammatory M1 polarization, while PT73 and PT55 scaffolds promoted anti-inflammatory M2 polarization at D2 and D3 stages. Thus, the dynamic changes in macrophage polarization and phenotype during degradation of bioresorbable scaffolds were confirmed *in vitro* for the first time. The effects of the degraded scaffolds on immunoregulation of osteogenesis were investigated by culturing effector cells with conditioned macrophage media. As reported previously, we observed the switch from M1 to M2 macrophages induced by PT55 scaffolds promoted osteogenesis, while maintenance of M1 polarization by PT37 scaffolds markedly suppressed osteogenesis [49,56].

To confirm the biological effects of the degraded scaffolds on macrophage polarization *in vivo*, we employed a subcutaneous implantation model to investigate the immune reactions to the implants [57]. Consistent with previous results, immunofluorescence staining further confirmed the sequential polarization from M1 to M2 macrophages from the D1 to D3 stage on PT73, PT64 and PT55 scaffolds, while PT37 scaffolds maintained M1 polarization.

To gain mechanistic insight into the biological mechanisms underlying the contrasting macrophage responses to degradation of different scaffolds, we performed RNA-Seq analysis of macrophages cultured with PT55 scaffolds and PT37 scaffolds at the mid-stage of degradation (D2). In addition to immune responses, inflammatory responses and macrophage differentiation, genes involved in other macrophages functions, such as organic substance metabolism, biosynthetic processes, regulation of phagocytosis and oxidation reduction processes, were significantly altered during scaffold degradation. Interestingly, KEGG pathway enrichment showed the phagosome pathway was also highly enriched in PT37 group.

Several research groups have previously reported that phagocytosis of DPs or particles results in inflammation, oxidative stress and M1 polarization, while the geometry of the DPs also influences macrophage phagocytosis [54,58,59]. TEM revealed masses of DPs engulfed by macrophages during the degradation process. Intracellular DPs were digested and disintegrated in phagosomes, and the DPs in macrophages co-cultured with PT46 and PT37 scaffolds resulted in aggregation of lysosomes. Our GO enrichment analysis indicated ROS-related processes were also activated by PT37 scaffolds. Previous studies also reported that the phagocytosis of micro- or nano-particles may induce oxidative stress [60,61]. Thus, this study indicates phagocytosis (endocytosis) of DPs from degraded scaffolds leads to ROS production and oxidative stress in macrophages. Flow cytometry and Western blot analysis confirmed that the levels of ROS and NOX2 expression were obviously enhanced by degraded PT37 scaffolds. Inhibition of endocytosis of phagocytosis using chlorpromazine or latrunculin B, respectively [62], both reduced NOX2 expression and M1 polarization of macrophages cultured on degraded PT37 scaffolds. These results suggest that the DPs of biodegradable materials might contribute to oxidative stress and M1 polarization of macrophages and may also lead to inflammation and the failure of bone healing.

Overall, this study indicates that addition of bio-active agents and/or enhancement of osteogenic ability may not be the most important factors in the design and manufacture of biodegradable bone tissue engineering scaffold. Changes in degradability of biomaterials may significantly alter the biological properties and effect of scaffolds during

the *in vivo* degradation process. Thus, through evaluation of the biological effects of materials during the entire degradation process on immune responses and bone regeneration is necessary in order to develop more promising material for bone regeneration.

5. Conclusions

Biodegradable PCL/ β -TCP scaffolds with a gradient of compositions (w/w, 70/30 to 30/70) were successfully fabricated through FDM. PT37 scaffolds with the highest TCP ceramic ratio had the best compressive modulus, hydrophilic performance, and angiogenic and osteogenic ability *in vitro*. However, the rapid rate of degradation of PT37 scaffolds disturbed the macrophage polarization process and led to a failure of bone healing *in vivo*. Using a dynamic *in vitro* degradation model, we identified that macrophages cultured with degraded PT37 scaffolds tended toward M1 polarization, while degraded PT73, PT64 and PT55 scaffolds induced M2 macrophage polarization. RNA-Seq revealed that phagocytosis of the DPs of PT scaffolds induces oxidative stress and M1 polarization of macrophages. Thus, this work indicates that it is necessary to carefully evaluate the potential biological effects of bone substitutes at each stage of degradation on immune responses and bone regeneration.

Conflict of interest

The authors declare no conflict of interest.

Data availability statement

All data that support the findings of this study are available on request from the corresponding author.

CRediT authorship contribution statement

Hao Wu: Writing – original draft, **Xinghui Wei:** Writing – original draft, **Yichao Liu:** Writing – original draft. **Hui Dong:** Formal analysis, **Zhen Tang:** Formal analysis, **Ning Wang:** Formal analysis. **Shusen Bao:** Formal analysis. **Zhigang Wu:** Methodology. **Lei Shi:** Investigation, Funding acquisition. **Xiongfei Zheng:** Resources, Investigation. **Xiaokang Li:** Conceptualization. **Zheng Guo:** Conceptualization.

Declaration of competing interest

The authors declare that they have no known competing financial interests or personal relationships that could have appeared to influence the work reported in this paper.

Acknowledgements

This work was financially supported by grants from the National Key Research and Development Program of China (grant number 2017YFC1104900) and The National Natural Science Foundation of China (No. 51871239, 51771227, 52171244 and 81772328). The authors also appreciate the support from the Incubation Project of the Army's Medical Technology Youth Cultivation Program of China (17QNP021). In addition, all authors sincerely appreciate the help of Engineer Hangfei Ren and Professor Yongquan Zhang from Wedo (Xian) Bio-Medical Technology Co., Ltd. designing the dynamic degradation reactor. Thanks to eceshi (www.eceshi.com) for the XRD, FTIR and GPC tests.

Appendix A. Supplementary data

Supplementary data to this article can be found online at <https://doi.org/10.1016/j.bioactmat.2022.07.032>.

References

- [1] A. Wubneh, E.K. Tsekoura, C. Ayranci, H. Uludag, Current state of fabrication technologies and materials for bone tissue engineering, *Acta Biomater.* 80 (2018) 1–30, <https://doi.org/10.1016/j.actbio.2018.09.031>.
- [2] L. Rosetti, V. Parisi, M. Petretta, C. Cavallo, G. Desando, I. Bartolotti, B. Grigolo, Scaffolds for bone tissue engineering: state of the art and new perspectives, *Mater. Sci. Eng. C. Mater. Biol. Appl.* 78 (2017) 1246–1262, <https://doi.org/10.1016/j.msec.2017.05.017>.
- [3] R. Agarwal, A.J. Garcia, Biomaterial strategies for engineering implants for enhanced osseointegration and bone repair, *Adv. Drug Deliv. Rev.* 94 (2015) 53–62, <https://doi.org/10.1016/j.addr.2015.03.013>.
- [4] J.O. Hollinger, G.C. Battistone, Biodegradable bone repair materials. Synthetic polymers and ceramics, *Clin. Orthop. Relat. Res.* 207 (1986) 290–305.
- [5] A. Bharadwaz, A.C. Jayasuriya, Recent trends in the application of widely used natural and synthetic polymer nanocomposites in bone tissue regeneration, *Mater. Sci. Eng. C. Mater. Biol. Appl.* 110 (2020), 110698, <https://doi.org/10.1016/j.msec.2020.110698>.
- [6] J.R. Porter, A. Henson, K.C. Papat, Biodegradable poly(epsilon-caprolactone) nanowires for bone tissue engineering applications, *Biomaterials* 30 (5) (2009) 780–788, <https://doi.org/10.1016/j.biomaterials.2008.10.022>.
- [7] E. Malikmammadov, T.E. Tanir, A. Kiziltay, V. Hasirci, N. Hasirci, PCL and PCL-based materials in biomedical applications, *J. Biomater. Sci. Polym. Ed.* 29 (7–9) (2018) 863–893, <https://doi.org/10.1080/09205063.2017.1394711>.
- [8] C. Yang, H. Ma, Z. Wang, M.R. Younis, C. Liu, C. Wu, Y. Luo, P. Huang, 3D printed wesselsite nanosheets functionalized scaffold facilitates NIR-II photothermal therapy and vascularized bone regeneration, *Adv. Sci.* 8 (20) (2021), e2100894, <https://doi.org/10.1002/advs.202100894>.
- [9] H. Liu, Y. Du, G. Yang, X. Hu, L. Wang, B. Liu, J. Wang, S. Zhang, Delivering proangiogenic factors from 3D-printed polycaprolactone scaffolds for vascularized bone regeneration, *Adv Healthc Mater* (2020), e2000727, <https://doi.org/10.1002/adhm.202000727>.
- [10] M.M. Shah, I. Ahmed, B. Marelli, C. Rudd, M.N. Bureau, S.N. Nazhat, Modulation of polycaprolactone composite properties through incorporation of mixed phosphate glass formulations, *Acta Biomater.* 6 (8) (2010) 3157–3168, <https://doi.org/10.1016/j.actbio.2010.03.002>.
- [11] H. Doyle, S. Lohfeld, P. Mchugh, Evaluating the effect of increasing ceramic content on the mechanical properties, material microstructure and degradation of selective laser sintered polycaprolactone/beta-tricalcium phosphate materials, *Med. Eng. Phys.* 37 (8) (2015) 767–776, <https://doi.org/10.1016/j.medengphy.2015.05.009>.
- [12] W.C. Lin, C. Yao, T.Y. Huang, S.J. Cheng, C.M. Tang, Long-term in vitro degradation behavior and biocompatibility of polycaprolactone/cobalt-substituted hydroxyapatite composite for bone tissue engineering, *Dent. Mater.* 35 (5) (2019) 751–762, <https://doi.org/10.1016/j.dental.2019.02.023>.
- [13] M. Alizadeh-Osgouei, Y. Li, C. Wen, A comprehensive review of biodegradable synthetic polymer-ceramic composites and their manufacture for biomedical applications, *Bioact. Mater.* 4 (1) (2019) 22–36, <https://doi.org/10.1016/j.bioactmat.2018.11.003>.
- [14] A. Malhotra, P. Habibovic, Calcium phosphates and angiogenesis: implications and advances for bone regeneration, *Trends Biotechnol.* 34 (12) (2016) 983–992, <https://doi.org/10.1016/j.tibtech.2016.07.005>.
- [15] P. Zhou, D. Xia, Z. Ni, T. Ou, Y. Wang, H. Zhang, L. Mao, K. Lin, S. Xu, J. Liu, Calcium silicate bioactive ceramics induce osteogenesis through oncostatin M, *Bioact. Mater.* 6 (3) (2021) 810–822, <https://doi.org/10.1016/j.bioactmat.2020.09.018>.
- [16] M. Li, X. Guo, W. Qi, Z. Wu, J.D. de Bruijn, Y. Xiao, C. Bao, H. Yuan, Macrophage polarization plays roles in bone formation instructed by calcium phosphate ceramics, *J. Mater. Chem. B* 8 (9) (2020) 1863–1877, <https://doi.org/10.1039/c9tb02932j>.
- [17] Y. Li, Z.G. Wu, X.K. Li, Z. Guo, S.H. Wu, Y.Q. Zhang, L. Shi, S.H. Teoh, Y.C. Liu, Z. Y. Zhang, A polycaprolactone-tricalcium phosphate composite scaffold as an autograft-free spinal fusion cage in a sheep model, *Biomaterials* 35 (22) (2014) 5647–5659, <https://doi.org/10.1016/j.biomaterials.2014.03.075>.
- [18] N. Wu, J. Liu, W. Ma, X. Dong, F. Wang, D. Yang, Y. Xu, Degradable calcium deficient hydroxyapatite/poly(lactic-glycolic acid copolymer) bilayer scaffold through integral molding 3D printing for bone defect repair, *Biofabrication* 13 (2) (2021), <https://doi.org/10.1088/1758-5090/abcb48>.
- [19] Y. Chen, J. Wang, X.D. Zhu, Z.R. Tang, X. Yang, Y.F. Tan, Y.J. Fan, X.D. Zhang, Enhanced effect of beta-tricalcium phosphate phase on neovascularization of porous calcium phosphate ceramics: in vitro and in vivo evidence, *Acta Biomater.* 11 (2015) 435–448, <https://doi.org/10.1016/j.actbio.2014.09.028>.
- [20] A. Bruyas, F. Lou, A.M. Stahl, M. Gardner, W. Maloney, S. Goodman, Y.P. Yang, Systematic characterization of 3D-printed PCL/beta-TCP scaffolds for biomedical devices and bone tissue engineering: influence of composition and porosity, *J. Mater. Res.* 33 (14) (2018) 1948–1959, <https://doi.org/10.1557/jmr.2018.112>.
- [21] C. Ma, Z. Ma, F. Yang, J. Wang, C. Liu, Poly(propylene fumarate)/beta-calcium phosphate composites for enhanced bone repair, *Biomater. Mater.* 14 (4) (2019), 45002, <https://doi.org/10.1088/1748-605X/ab12ae>.
- [22] L. Lu, Q. Zhang, D. Wootton, R. Chiou, D. Li, B. Lu, P. Lelkes, J. Zhou, Biocompatibility and biodegradation studies of PCL/beta-TCP bone tissue scaffold fabricated by structural porogen method, *J. Mater. Sci. Mater. Med.* 23 (9) (2012) 2217–2226, <https://doi.org/10.1007/s10856-012-4695-2>.
- [23] S.H. Park, E.S. Gil, H.J. Kim, K. Lee, D.L. Kaplan, Relationships between degradation of silk scaffolds and osteogenesis, *Biomaterials* 31 (24) (2010) 6162–6172, <https://doi.org/10.1016/j.biomaterials.2010.04.028>.

- [24] Y. Peng, Q.J. Liu, T. He, K. Ye, X. Yao, J. Ding, Degradation rate affords a dynamic cue to regulate stem cells beyond varied matrix stiffness, *Biomaterials* 178 (2018) 467–480, <https://doi.org/10.1016/j.biomaterials.2018.04.021>.
- [25] J. Han, P. Wan, Y. Ge, X. Fan, L. Tan, J. Li, K. Yang, Tailoring the degradation and biological response of a magnesium-strontium alloy for potential bone substitute application, *Mater. Sci. Eng. C. Mater. Biol. Appl.* 58 (2016) 799–811, <https://doi.org/10.1016/j.msec.2015.09.057>.
- [26] D. Yang, J. Xiao, B. Wang, L. Li, X. Kong, J. Liao, The immune reaction and degradation fate of scaffold in cartilage/bone tissue engineering, *Mater. Sci. Eng. C. Mater. Biol. Appl.* 104 (2019), 109927, <https://doi.org/10.1016/j.msec.2019.109927>.
- [27] J.E. Bergsma, F.R. Rozema, R.R. Bos, G. Boering, W.C. de Bruijn, A.J. Pennings, In vivo degradation and biocompatibility study of in vitro pre-degraded as-polymerized polyactide particles, *Biomaterials* 16 (4) (1995) 267–274, [https://doi.org/10.1016/0142-9612\(95\)93253-a](https://doi.org/10.1016/0142-9612(95)93253-a).
- [28] J. Ping, C. Zhou, Y. Dong, X. Wu, X. Huang, B. Sun, B. Zeng, F. Xu, W. Liang, Modulating immune microenvironment during bone repair using biomaterials: focusing on the role of macrophages, *Mol. Immunol.* 138 (2021) 110–120, <https://doi.org/10.1016/j.molimm.2021.08.003>.
- [29] C. Schlundt, H. Fischer, C.H. Bucher, C. Rendenbach, G.N. Duda, K. Schmidt-Bleek, The multifaceted roles of macrophages in bone regeneration: a story of polarization, activation and time, *Acta Biomater.* 133 (2021) 46–57, <https://doi.org/10.1016/j.actbio.2021.04.052>.
- [30] H. Wei, J. Cui, K. Lin, J. Xie, X. Wang, Recent advances in smart stimuli-responsive biomaterials for bone therapeutics and regeneration, *Bone Res* 10 (1) (2022) 17, <https://doi.org/10.1038/s41413-021-00180-y>.
- [31] Y. Li, L. Yang, Y. Hou, Z. Zhang, M. Chen, M. Wang, J. Liu, J. Wang, Z. Zhao, C. Xie, X. Lu, Polydopamine-mediated graphene oxide and nanohydroxyapatite-incorporated conductive scaffold with an immunomodulatory ability accelerates periodontal bone regeneration in diabetes, *Bioact. Mater.* 18 (2022) 213–227, <https://doi.org/10.1016/j.bioactmat.2022.03.021>.
- [32] Y. Wang, H. Huang, G. Jia, H. Zeng, G. Yuan, Fatigue and dynamic biodegradation behavior of additively manufactured Mg scaffolds, *Acta Biomater.* 135 (2021) 705–722, <https://doi.org/10.1016/j.actbio.2021.08.040>.
- [33] W.B. Swanson, M. Omi, Z. Zhang, H.K. Nam, Y. Jung, G. Wang, P.X. Ma, N. E. Hatch, Y. Mishina, Macropore design of tissue engineering scaffolds regulates mesenchymal stem cell differentiation fate, *Biomaterials* 272 (2021), 120769, <https://doi.org/10.1016/j.biomaterials.2021.120769>.
- [34] E. Malikmammadov, T.E. Tanir, A. Kiziltay, V. Hasirci, N. Hasirci, PCL and PCL-based materials in biomedical applications, *J. Biomater. Sci. Polym. Ed.* 29 (7–9) (2018) 863–893, <https://doi.org/10.1080/09205063.2017.1394711>.
- [35] H. Sun, L. Mei, C. Song, X. Cui, P. Wang, The in vivo degradation, absorption and excretion of PCL-based implant, *Biomaterials* 27 (9) (2006) 1735–1740, <https://doi.org/10.1016/j.biomaterials.2005.09.019>.
- [36] Y. Zhang, J. Cao, X. Wang, H. Liu, Y. Shao, C. Chu, F. Xue, J. Bai, The effect of enzymes on the in vitro degradation behavior of Mg alloy wires in simulated gastric fluid and intestinal fluid, *Bioact. Mater.* 7 (2022) 217–226, <https://doi.org/10.1016/j.bioactmat.2021.05.047>.
- [37] P.A. Mouthuy, S. Snelling, S.G. Dakin, L. Milkovic, A.C. Gasparovic, A.J. Carr, N. Zarkovic, Biocompatibility of implantable materials: an oxidative stress viewpoint, *Biomaterials* 109 (2016) 55–68, <https://doi.org/10.1016/j.biomaterials.2016.09.010>.
- [38] M. Bruggmans, S. Sntjens, M. Cox, A. Nandakumar, A.W. Bosman, T. Mes, H. M. Janssen, C. Bouten, F. Baaijens, A. Driessen-Mol, Hydrolytic and oxidative degradation of electrospun supramolecular biomaterials: in vitro degradation pathways, *Acta Biomater.* 27 (2015) 21–31, <https://doi.org/10.1016/j.actbio.2015.08.034>.
- [39] C.X. Lam, S.H. Teoh, D.W. Huttmacher, Comparison of the degradation of polycaprolactone and polycaprolactone-(β -tricalcium phosphate) scaffolds in alkaline medium, *Polym. Int.* 56 (6) (2007) 718–728, <https://doi.org/10.1002/pi.2195>.
- [40] C.X. Lam, M.M. Savalani, S.H. Teoh, D.W. Huttmacher, Dynamics of in vitro polymer degradation of polycaprolactone-based scaffolds: accelerated versus simulated physiological conditions, *Biomed. Mater.* 3 (3) (2008), 34108, <https://doi.org/10.1088/1748-6041/3/3/034108>.
- [41] F. Zhao, B. van Rietbergen, K. Ito, S. Hofmann, Flow rates in perfusion bioreactors to maximise mineralisation in bone tissue engineering in vitro, *J. Biomech.* 79 (2018) 232–237, <https://doi.org/10.1016/j.jbiomech.2018.08.004>.
- [42] H.S. Han, I. Jun, H.K. Seok, K.S. Lee, K. Lee, F. Witte, D. Mantovani, Y.C. Kim, S. Glyn-Jones, J.R. Edwards, Biodegradable magnesium alloys promote angiogenesis to enhance bone repair, *Adv. Sci.* 7 (15) (2020), 2000800, <https://doi.org/10.1002/adv.202008000>.
- [43] W. Li, W. Qiao, X. Liu, D. Bian, D. Shen, Y. Zheng, J. Wu, K. Kwan, T.M. Wong, K. Cheung, K. Yeung, Biomimicking bone-implant interface facilitates the bioadaptation of a new degradable magnesium alloy to the bone tissue microenvironment, *Adv. Sci.* 8 (23) (2021), e2102035, <https://doi.org/10.1002/adv.202102035>.
- [44] R.J. Miron, H. Zohdi, M. Fujioka-Kobayashi, D.D. Bosshardt, Giant cells around bone biomaterials: osteoclasts or multi-nucleated giant cells? *Acta Biomater.* 46 (2016) 15–28, <https://doi.org/10.1016/j.actbio.2016.09.029>.
- [45] M. Barbeck, P. Booms, R. Unger, V. Hoffmann, R. Sader, C.J. Kirkpatrick, S. Ghanaati, Multinucleated giant cells in the implant bed of bone substitutes are foreign body giant cells—New insights into the material-mediated healing process, *J. Biomed. Mater. Res.* 105 (4) (2017) 1105–1111, <https://doi.org/10.1002/jbm.a.36006>.
- [46] Y. Song, L. Li, W. Zhao, Y. Qian, L. Dong, Y. Fang, L. Yang, Y. Fan, Surface modification of electrospun fibers with mechano-growth factor for mitigating the foreign-body reaction, *Bioact. Mater.* 6 (9) (2021) 2983–2998, <https://doi.org/10.1016/j.bioactmat.2021.02.020>.
- [47] H. Atcha, A. Jairaman, J.R. Holt, V.S. Meli, R.R. Nagalla, P.K. Veerasubramanian, K.T. Brumm, H.E. Lim, S. Othy, M.D. Cahalan, M.M. Pathak, W.F. Liu, Mechanically activated ion channel Piezo1 modulates macrophage polarization and stiffness sensing, *Nat. Commun.* 12 (1) (2021) 3256, <https://doi.org/10.1038/s41467-021-23482-5>.
- [48] N. Jain, J. Moeller, V. Vogel, Mechanobiology of macrophages: how physical factors coregulate macrophage plasticity and phagocytosis, *Annu. Rev. Biomed. Eng.* 21 (2019) 267–297, <https://doi.org/10.1146/annurev-bioeng-062117-121224>.
- [49] W. Qiao, H. Xie, J. Fang, J. Shen, W. Li, D. Shen, J. Wu, S. Wu, X. Liu, Y. Zheng, K. Cheung, K. Yeung, Sequential activation of heterogeneous macrophage phenotypes is essential for biomaterials-induced bone regeneration, *Biomaterials* 276 (2021), 121038, <https://doi.org/10.1016/j.biomaterials.2021.121038>.
- [50] J. Lee, H. Byun, P.S. Madhurakkat, S. Lee, H. Shin, Current advances in immunomodulatory biomaterials for bone regeneration, *Adv Healthc Mater* 8 (4) (2019), e1801106, <https://doi.org/10.1002/adhm.201801106>.
- [51] L. Li, Q. Li, L. Gui, Y. Deng, L. Wang, J. Jiao, Y. Hu, X. Lan, J. Hou, Y. Li, D. Lu, Sequential gastrin release PU/n-HA composite scaffolds reprogram macrophages for improved osteogenesis and angiogenesis, *Bioact. Mater.* 19 (2023) 24–37, <https://doi.org/10.1016/j.bioactmat.2022.03.037>.
- [52] Y. Peng, Q.J. Liu, T. He, K. Ye, X. Yao, J. Ding, Degradation rate affords a dynamic cue to regulate stem cells beyond varied matrix stiffness, *Biomaterials* 178 (2018) 467–480, <https://doi.org/10.1016/j.biomaterials.2018.04.021>.
- [53] H. Pan, H. Jiang, W. Chen, The biodegradability of electrospun Dextran/PLGA scaffold in a fibroblast/macrophage co-culture, *Biomaterials* 29 (11) (2008) 1583–1592, <https://doi.org/10.1016/j.biomaterials.2007.12.005>.
- [54] L. Jin, C. Chen, G. Jia, Y. Li, J. Zhang, H. Huang, B. Kang, G. Yuan, H. Zeng, T. Chen, The bioeffects of degradable products derived from a biodegradable Mg-based alloy in macrophages via heterophagy, *Acta Biomater.* 106 (2020) 428–438, <https://doi.org/10.1016/j.actbio.2020.02.002>.
- [55] F.Y. Mcwhorter, T. Wang, P. Nguyen, T. Chung, W.F. Liu, Modulation of macrophage phenotype by cell shape, *Proc. Natl. Acad. Sci. U. S. A.* 110 (43) (2013) 17253–17258, <https://doi.org/10.1073/pnas.1308887110>.
- [56] L. Chen, D. Wang, J. Qiu, X. Zhang, X. Liu, Y. Qiao, X. Liu, Synergistic effects of immunoregulation and osteoinduction of ds-block elements on titanium surface, *Bioact. Mater.* 6 (1) (2021) 191–207, <https://doi.org/10.1016/j.bioactmat.2020.08.001>.
- [57] I. Flaig, M. Radenkovic, S. Najman, A. Prohl, O. Jung, M. Barbeck, In vivo analysis of the biocompatibility and immune response of jellyfish collagen scaffolds and its suitability for bone regeneration, *Int. J. Mol. Sci.* 21 (12) (2020), <https://doi.org/10.3390/ijms21124518>.
- [58] J.A. Champion, S. Mitragotri, Role of target geometry in phagocytosis, *Proc. Natl. Acad. Sci. U. S. A.* 103 (13) (2006) 4930–4934, <https://doi.org/10.1073/pnas.0600997103>.
- [59] W.W. Jiang, S.H. Su, R.C. Eberhart, L. Tang, Phagocyte responses to degradable polymers, *J. Biomed. Mater. Res.* 82 (2) (2007) 492–497, <https://doi.org/10.1002/jbm.a.31175>.
- [60] X. Wang, C.H. Chang, J. Jiang, Q. Liu, Y.P. Liao, J. Lu, L. Li, X. Liu, J. Kim, A. Ahmed, A.E. Nel, T. Xia, The crystallinity and aspect ratio of cellulose nanomaterials determine their pro-inflammatory and immune adjuvant effects in vitro and in vivo, *Small* 15 (42) (2019), e1901642, <https://doi.org/10.1002/sml.201901642>.
- [61] J. Ding, R. Venkatesan, Z. Zhai, W. Muhammad, J.R. Nakkala, C. Gao, Micro- and nanoparticles-based immunoregulation of macrophages for tissue repair and regeneration, *Colloids Surf. B Biointerfaces* 192 (2020), 111075, <https://doi.org/10.1016/j.colsurfb.2020.111075>.
- [62] H. Li, K. Tatamatsu, M. Somya, M. Iijima, S. Kuroda, Development of a macrophage-targeting and phagocytosis-inducing bio-nanocapsule-based nanocarrier for drug delivery, *Acta Biomater.* 73 (2018) 412–423, <https://doi.org/10.1016/j.actbio.2018.04.023>.